

MECHANISMS OF CELL DEATH CAUSED BY PHOTOTHERMAL ABLATION
OF CANCER CELLS MEDIATED BY CONDUCTIVE POLYMER
NANOPARTICLES

By

Madeline Elaine Huff, B.S.

A thesis submitted to the Graduate Council of
Texas State University in partial fulfillment
of the requirements for the degree of
Master of Science
with a Major in Biochemistry
May 2018

Committee Members:

Tania Betancourt, Chair

Liqin Du

L. Kevin Lewis

COPYRIGHT

by

Madeline Elaine Huff

2018

FAIR USE AND AUTHOR'S PERMISSION STATEMENT

Fair Use

This work is protected by the Copyright Laws of the United States (Public Law 94-553, section 107). Consistent with fair use as defined in the Copyright Laws, brief quotations from this material are allowed with proper acknowledgement. Use of this material for financial gain without the author's express written permission is not allowed.

Duplication Permission

As the copyright holder of this work I, Madeline Elaine Huff, refuse permission to copy in excess of the "Fair Use" exemption without my written permission.

DEDICATION

To Mom and Dad, for which none of this would have been possible.

To Victor, for letting me practice three years-worth of presentations on you. This would not have been easy without you.

To Ale, we did it!

ACKNOWLEDGEMENTS

There are many people whom have helped me get to where I am right now, therefore I have quite a few people to acknowledge:

First of all, I would like to acknowledge all of the Chemistry and Biochemistry Department's faculty. All of my professors throughout my undergraduate and graduate career created a comfortable and exciting learning environment that helped me excel in my thesis work.

I would also like to acknowledge out collaborators, Dr. Jennifer Irvin and Dr. James Tunnell. A big thank you to Dr. James Tunnell for allowing me to work in his lab for a good three months while conducting my flow cytometry experiments.

I would like to give a big shout out to all the individuals in the Betancourt lab, both past and currents lab-mates. Thank you Tugba and Janet for being the first individuals to welcome, teach, and train me in the lab. Thank you Gaby for always keeping me company during those late night experiments and for always making things just a little more fun and interesting.

Lastly, and most importantly, I would like to thank and acknowledge my advisor Dr. Tania Betancourt. I am beyond thankful that I decided to join this lab when I was an undergraduate student, and I contribute the majority of the success I achieved during my graduate years to you. The experience I gained working for you definitely helped shape both myself as a biochemist and my future as a whole. Thank you for being such an inspirational mentor in my life.

TABLE OF CONTENTS

	Page
ACKNOWLEDGEMENTS	v
LIST OF TABLES.....	viii
LIST OF FIGURES.....	ix
CHAPTER	
I. INTRODUCTION	1
1.1 Objectives of Research.....	1
1.2 Background	5
1.2.1 Passive and Active Delivery of Nanomedicines.....	5
1.2.2 Photothermal Therapy.....	7
1.2.3 Conductive Polymer Nanoparticles	10
1.2.4 Combination Therapy.....	12
1.2.5 Cell Death Mechanisms	15
II. MATERIALS AND METHODS	20
2.1 Materials.....	20
2.2 Monomer Purification.....	20
2.3 Synthesis of poly(3,4-ethylenedioxythiophene) (PEDOT) NPs.....	21
2.4 Characterization of PEDOT NPs.....	23
2.5 Effect of PEDOT NPs on Laser-Induced PTT	24
2.6 Cell Culture	25
2.7 Cell Internalization	25
2.8 Photothermal Effect on Cell Death.....	27
2.9 Photothermal Effect on Caspase-3/7 Expression.....	29
2.10 Image Quantification.....	30
2.11 Flow Cytometry	30
2.12 Statistical Analysis.....	32

III. RESULTS	33
3.1 PEDOT and PEDOT/NR NP Characterization	33
3.2 Photothermal Effect of PEDOT NPs	36
3.3 Cellular Internalization of PEDOT NPs.....	37
3.4 Qualitative Analysis of Cell Death by Fluorescence Microscopy.....	39
3.5 Quantitative Analysis of Cell Death by Flow Cytometry	46
3.6 Caspase Expression in Cell Death	52
IV. DISCUSSION AND CONCLUSION	56
4.1 Discussion	56
4.2 Conclusions	60
APPENDIX.....	62
REFERENCES.....	63

LIST OF TABLES

Table	Page
1. Excitation and Emission Wavelengths of Fluorescently Labeled Biochemical Reagents and Compatible Filter Cubes	28
2. Size, PDI, and Zeta Potential of PEDOT and PEDOT/NR NPs.....	35
3. R ² values for each irradiation time period.....	37

LIST OF FIGURES

Figure	Page
1. Photothermal Heating of Passively Targeted Gold Nanorod Antennas in Tumors.....	10
2. Targeting Silica-Encapsulated Gold Nanorods for Chemo/Photothermal Therapy	14
3. Schematic of PEDOT NP Preparation	23
4. Excitation and Emission Spectra of Calcein Blue AM, AlexaFluor 488, and Propidium Iodide	28
5. PEDOT and PEDOT/NR NP Synthesis.....	33
6. PEDOT NP Characterization.....	35
7. Temperature change (°C) as a function of NP concentration ($\mu\text{g/ml}$) after 1, 5, and 15 minutes of irradiation using an 808-nm laser at 3.0 W/cm^2	37
8. Confocal microscopy images of MDA-MB-231 cell co-incubated with $500 \mu\text{g/ml}$ concentrations of PEDOT/NR NPs for 1.5 and 24-hour time periods.....	39
9. Fluorescence Microscopy Images of Control Samples.....	40
10. Fluorescence Microscopy of Cells Exposed to NPs for 1.5 Hours and Irradiation with an 808-nm Laser.....	42
11. Fluorescence Microscopy of Cells Exposed to NPs for 6 Hours and Irradiation with an 808-nm Laser.....	43
12. Fluorescence Microscopy of Cells Exposed to NPs for 12 Hours and Irradiation with an 808-nm Laser.....	44

13. Fluorescence Microscopy of Cells Exposed to NPs for 24 Hours and Irradiation with an 808-nm Laser.....	45
14. Flow Cytometry region determination.....	47
15. Quantitative Analysis of Cell Death Pathways by Flow Cytometry	49
16. Flow Cytometry Data After NP Incubation Period and Irradiation with an 808-nm Laser	50
17. Fluorescence Microscopy Images of Caspase-3/7 Expression in Cell Populations After 1.5 Hours of Co-Incubation with NPs and Irradiation with an 808-nm Laser ...	53
18. Fluorescence Microscopy Images of Caspase-3/7 Expression in Cell Populations After 24 Hours of Co-Incubation with NPs and Irradiation with an 808-nm Laser	54
19. Fluorescence Density Indicative of Caspase 3/7 Expression	55

Chapter I

INTRODUCTION

1.1 Objectives of Research

Cancer is the second leading cause of death in the United States and a major public health concern worldwide.¹ The diagnoses of 1,688,780 new cancer cases are projected to occur in 2017, the equivalent of more than 4,600 new cases each day.¹ Breast cancer alone is expected to account for 30% of all new cancer diagnoses in women, with an estimate of 40,610 deaths this year.¹ The most common treatment options for cancer diagnosis include surgery, radiation, and chemotherapy. While these therapies have proven somewhat effective, the use of radiation therapy and chemotherapy for late stage cancer treatments is highly restrained due to the irreparable damage that occurs, not only to the targeted malignant cancerous cells, but also to the healthy tissue within the body.² Off-target toxicity is a major limitation that compromises the effectiveness of chemotherapeutic treatment, and has left the need for a less systematically invasive and more effective treatment option.^{4,5,6} The ultimate goal in the battle against cancer has been to develop an effective therapeutic strategy that is high in specificity and low in toxicity for the eradication of tumors.³ These treatments have not only failed in this goal, but frequently lead to the chronic side effects of cardiomyopathy, neuropathy, and an increased risk of developing a secondary cancer.^{7,8}

The emerging field of theranostics has aimed to provide a more specific and individualized treatment for heterogeneous diseases, such as cancer, by combining molecular diagnostics and targeted therapeutics into a single agent.^{9,10} The development

of nanotechnology has played a vital role in theranostic nanomedicine by utilizing nanoplateforms to overcome the limitations faced by invasive imaging/detection methods and traditional therapeutic options, such as chemotherapy. This single nanoagent is capable of accomplishing the ultimate goal in the battle of cancer by offering a balance between reduced toxicity and therapeutic efficacy.¹¹ The attraction of nanoparticles for medical purposes stems from their relatively large surface area which is able to bind, absorb, and carry other compounds such as drugs, probes, and proteins for targeted delivery. Once introduced into the body, nanoparticles within a certain size range (5 – 100 nm) have demonstrated strong interactions with biomolecules, such as enzymes and receptors, both inside the cell and on the surface.¹² Molecularly conjugated nanoparticles are capable of binding and interacting with specific cellular receptors for selective detection and treatment.¹³ Many efforts in research have been placed on the goal of personalized medicine, most commonly utilizing the passive accumulation of nanoparticles in tumor cells via the Enhanced Permeability and Retention (EPR) effect for the theranostic applications of fluorescence imaging, image-guided resection, localized drug delivery, and photothermal therapy (PTT).¹⁴

The use of near-infrared (NIR) light to excite nanoparticles as photothermal agents has proven to be an effective and highly selective method in the ablation of cancer cells by the rapid increase of heat to intolerable temperatures. Our laboratory has previously developed conductive polymer nanoparticles that absorb light in the near infrared region and have demonstrated their potential as cytocompatible, yet effective agents for photothermal ablation of breast cancer cells.^{15,16} While gold nanorods and nanoshells have been explored extensively as photothermal agents,^{24,25,43} conductive

polymer nanoparticles have only recently been explored as alternative agents for photothermal ablation.³³ Hence, there is not a good understanding of the mechanisms of cell death associated with these new types of nanoparticles with the target tumor tissues.

The goal of this research was to investigate and develop a better understanding of the specific cell death mechanisms caused by NIR laser-induced ablation of MDA-MB-231 breast cancer cells in order to increase the efficacy of conductive polymer nanoparticle-mediated PTT. A biochemical investigation of the cancer cells after PTT was carried out to aid in the differentiation between the two most common types of cell death, apoptosis and necrosis. The fluorescent biochemical markers that act as indicators of these types of cell death were assessed as a function of nanoparticle concentration, nanoparticle-cell incubation time, and laser irradiation time. Controls consisted of live cells without any treatment, induced necrotic cells, induced apoptotic cells, live cells exposed to irradiation without nanoparticles, and live cells exposed to nanoparticles without irradiation. The objective was to use polymeric nanoparticles as photothermal agents that can accumulate within the cancer cells and induce ablation when stimulated by NIR light. As a response to the stimulus, we monitored whether apoptosis or necrosis occurred independently, sequentially, or simultaneously. The central hypothesis of this research was that interaction of nanoparticles within breast cancer cells will activate distinct cell death pathways as a result of photothermal ablation and the various experimental parameters being tested.

To accomplish these goals, the following objectives were achieved:

1. **Synthesis and characterization of conductive polymer nanoparticles.**

Photothermal agents were prepared from 3,4-ethylenedioxythiophene (EDOT)

monomer using a two-surfactant oxidative-emulsion polymerization process, yielding a colloidal and aqueous suspension of poly(3,4-ethylenedioxythiophene) (PEDOT) nanoparticles. UV/VIS/NIR absorption spectroscopy was used to confirm strong absorption of the PEDOT nanoparticles in the NIR region. Dynamic light scattering and zeta potential analysis were performed to validate the size and zeta potential of the nanoparticles. Adequate temperature change as a function of nanoparticle concentration and laser irradiation time in the absence of cells was verified for the photothermal ablation agents.

2. **Qualitative analysis of cell death by fluorescence microscopy.** Annexin V AlexaFluor 488, Propidium Iodide, and Calcein Blue AM were utilized as fluorescent biochemical markers after exposure to nanoparticles and irradiation with a NIR laser. Annexin V 488 detects translocated phosphatidylserine, which is indicated by its extracellular exposure on the plasma membrane of cells undergoing early to intermediate stages of apoptosis. In conjunction with Annexin V 488, Propidium Iodide (PI) is a nucleic acid stain that is able to accurately assess mixed cell populations that also display cells undergoing necrotic death, where the compromised cell membrane allows for the passage of the fluorescent PI dye into the nucleus. Calcein Blue AM presents live cells that display enzymatic activity, having maximal fluorescence upon cleavage of the acetomethyl (AM) ester by intracellular esterases. A caspase-3 detection reagent was used to confirm

apoptotic cells by the cleavage of a fluorogenic substrate by activated caspase-3.

3. **Quantitative analysis of cell death by flow cytometry.** The previously presented fluorophores were utilized for quantification of treated cancer cells by flow cytometry. The biomarkers were detected for each experimental variable.

The expected outcomes from this study include a more thorough comprehension of the cellular response of breast cancer cells upon laser-induced photothermal treatment with polymeric nano-agents, which is expected to be a complex mechanism that depends highly on the dose as well as on the amount of optical energy absorbed and subsequently dissipated by the nanoparticles. Insight into the mechanisms of cell death caused by photothermal therapy provides the foundation to predict and optimize the parameters of this specific, controlled, and localized treatment of cancer for the advancement of modern nanomedicine.

1.2 Background

1.2.1 Passive and Active Delivery of Nanomedicines

The optimal intravenously administered nanoparticles should be between 10 and 100 nm in diameter to increase half-life circulation time, as larger nanoparticles are removed primarily by the spleen and liver, and smaller particles by the renal system.²³ Circulating macrophages and resident reticuloendothelial cells in the spleen and liver

recognize these particles as foreign, resulting in the engulfment and clearance from circulation.

Passive targeting takes advantage of the unique and imperfect characteristics exhibited by tumor microenvironments. When nanoparticles are administered intravenously, the nanoparticles can preferentially accumulate in tumors via the enhanced permeability and retention (EPR) effect, where particles less than a couple hundred nanometers passively eject through wide fenestrations that are characteristic of the highly disorganized vasculature that forms once the tumor undergoes rapid angiogenesis.²⁴ Angiogenesis, or the development of new blood vessels, occurs once the tumor grows large enough to start requiring more nutrients and oxygen, which leads to the development of imperfect and “leaky” vessels.²⁵ The nanoparticles are then retained within the tumor environment due to an underdeveloped lymphatic drainage system, which is unable to efficiently clear them out of the tumor.¹⁷

In contrast, active targeting utilizes molecularly functionalized nanoparticles that can typically reach target tumor cells through ligand-receptor interactions that induce clathrin-mediated endocytosis.²⁴ Affinity ligands, such as antibodies, aptamers, peptides, or small molecules, can be attached to the surface of nano-agents through various conjugation methods and allow for the targeting of specific receptors on the cell surface.²⁶ Ideally, the targeted cellular receptors should be overexpressed on the surface of tumor cells and not normal cells in order to achieve high specificity.²⁶

Nanoparticle-mediated photothermal therapy has exploited both the poor vasculature of tumors and the EPR effect for the localized destruction of cancer cells,

while also enhancing other therapeutic approaches, such as chemotherapy, for a synergistic cancer killing effect.²⁵

1.2.2 Photothermal Therapy

Photothermal therapy is a form of highly regulated nanoparticle-mediated hyperthermia, where the treatment occurs in a confined region and allows for minimal damage to the surrounding healthy tissue.⁵ Hyperthermia is defined as a noninvasive anticancer approach in which biological tissues are exposed to an increase in temperature within the range of 41-50°C, with the induction of cancer cell death occurring at temperatures as low as 42°C.¹⁷ Tumors are destroyed in this temperature range because of their reduced heat tolerance compared to normal tissue, which can be due to the inhibition of oxidative metabolism causing a lower cellular pH.¹⁸

Photoabsorbing agents are able to convert absorbed light to thermal heat, leading to the ablation of cancer cells and the subsequent cell death.¹⁹ Ideal photothermal agents should absorb in the near infrared (NIR) region (700-1000 nm), which is the optimal range of wavelengths in the electromagnetic spectrum where light has the maximum depth of penetration in tissue.²⁰ Water, melanin, and hemoglobin have minimal absorbance in this therapeutic window of wavelengths, which enables light to penetrate easily for *in vivo* therapy of tumors deep within the tissue.¹⁵ When photothermal agents absorb NIR light, electrons transition from the ground state to an excited state. This results in an increase in kinetic energy, leading to the overheating of the local environment the nanoparticles reside within.²¹ Additionally, photothermal agents should

be nontoxic and have a high tumor affinity in order to improve therapeutic efficacy without rendering toxic side effects.

For the past two decades, advancements in nanotechnology have given rise to a variety of strong NIR-absorbing nanoparticles for photothermal treatment of cancer, achieving high therapeutic efficacies in many *in vivo* studies.^{24,29} Inorganic nanomaterials have been heavily studied for their specificity and sensitivity as PTT agents, including various gold nanostructures³⁷, carbon nanostructures³⁶, palladium nanosheets³⁸, and iron oxide nanoparticles³⁹. Organic nanoparticles include conjugated polymers¹⁵, porphyrins²⁷, and micelle-encapsulated NIR dyes²⁸. Gold nanostructures have been the most extensively explored for both cancer diagnosis and therapy because of their easily tunable absorbance spectra and the reasonable biocompatibility of the inert element of gold.²⁹

Gold nanoshells were the first nano-agent to be investigated for their photothermal properties and used to demonstrate photothermal cancer therapy.²⁹ Gold nanoshells were invented in the mid-1990's by Rice researchers Dr. Naomi Halas and Dr. Jennifer West, founders of the company Nanospectra Biosciences, Inc. The nanoshells consist of a gold shell formed on top of a dielectric silica core, and can easily be tuned to the NIR region by modifying the thickness of the shell.³⁰ When first tested in mice, nanoshell-treated tumors resulted in a temperature increase of 37.4°C when exposed to NIR light for 4-6 minutes. The result was tumor remission in 100% of the experimental subjects with minimal effect on healthy tissues.³¹ Cancer Treatment Centers of America (CTCA) and Nanospectra Biosciences are performing the first FDA approved clinical

trials for the treatment of head, neck, and lung cancer by photothermal therapy using gold nanoshells.^{32,33}

Gold nanorods have also seen successful therapeutic efficacy in the case of *in vivo* photothermal therapy. Maltzahn et al. demonstrated that polyethylene glycol (PEG)-coated gold nanorods (PEG-NR) had a long bloodstream circulation time of ~17 hours after intravenous injection into tumor-bearing mice, with the nanorods accumulating in the tumor at approximately 7% injected dose/gram tissue at 72 hours post injection.³⁴ The tumors on the mice that were intravenously injected with the gold nanorods rapidly heated to over 70°C after 5 minutes of NIR laser irradiation at 2 W/cm² (Figure 1).³⁴ The tumors on the mice completely disappeared within 10 days of treatment, with the control groups still showing prominent tumor growth.³⁴

Various nanoparticles have been evaluated and have seen similar successful therapeutic efficacies, including silica nanoparticles,³⁵ carbon nanotubes,³⁶ gold nanoparticles,³⁷ quantum dots,³⁸ and iron oxide nanoparticles.³⁹ However, conductive polymer nanoparticles have only recently been explored as alternative agents for photothermal ablation of cancer cells due to their ability to be adjusted to absorb radiation in the NIR region.^{15,16}

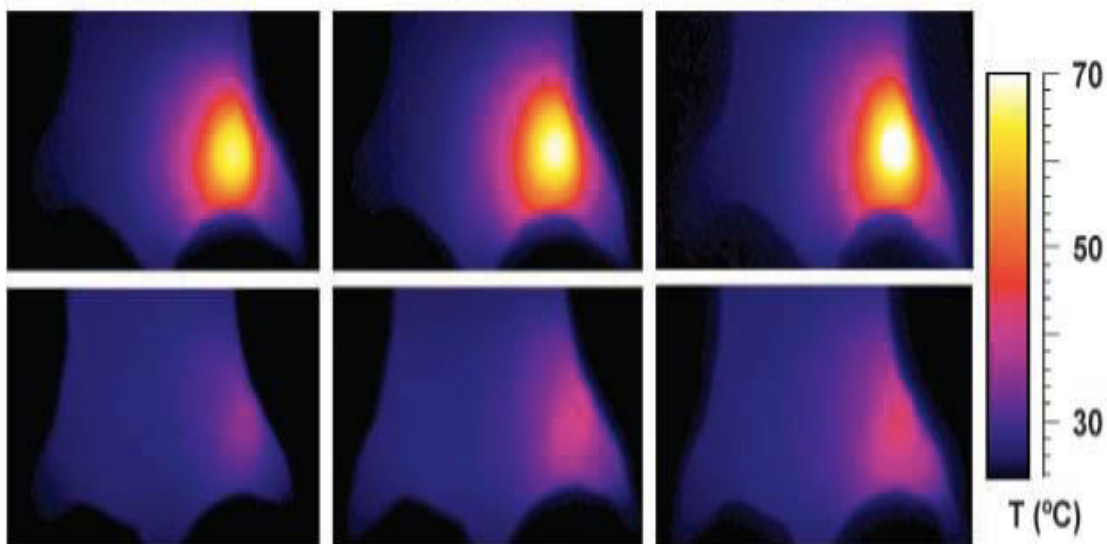


Figure 1. Photothermal Heating of Passively Targeted Gold Nanorod Antennas in Tumors. Thermographic surveillance of photothermal heating in PEG-NR-injected (top) and saline-injected (bottom) mice. Reference 34.

1.2.3 Conductive Polymer Nanoparticles

Conductive polymers that contain conjugated molecular structures have been widely used in many different areas for applications such as organic conductors and electroluminescence diodes, but only recently have been investigated as photothermal agents.⁴⁰ Yang et al. demonstrated the practicability of a novel organic photothermal agent based on polyaniline for the induction of hyperthermia in epithelial cancer.⁴¹ During the doping process, the optical-absorbance peak of polyaniline was red-shifted toward the NIR region as a result of its transition from the emeraldine base to the emeraldine salt. The photothermal efficiency of the conductive polyaniline nanoparticles was evaluated using 2.45 W/cm^2 for 5 minutes, showing a highly effective and feasible photothermal ablation effect both *in vitro* and *in vivo*.⁴¹ In 2012, Cheng et al. investigated PEGylated poly(ethylenedioxythiophene):poly(4-styrenesulfonate)(PEDOT:PSS) nanoparticles as another novel class of conjugated polymer nanoparticles utilized for

photothermal ablation of cancer cells. The PEDOT:PSS-PEG nanoparticles had an average diameter of 80 nm and were highly stable in the physiological environment. *In vivo* PTT studies were carried out in mice bearing 4T1 tumors. After IV injection of PEDOT:PSS-PEG nanoparticles, the mice were treated to 0.5 W/cm² of NIR light for 5 minutes. The treatment completely eradicated the tumors on treated mice. The potential toxicology of these nanoparticles was also studied *in vivo*. All measures fell within normal range, evidencing that PEDOT:PSS-PEG nanoparticles were not noticeably toxic *in vivo* to the mice at the tested dose.⁴²

In prior work from our group, the photothermal conversion efficiencies of conductive polymer nanoparticles have been found to be greater than both gold nanorods and gold nanoshells.¹⁶ The conversion efficiency of conductive polymer nanoparticles was greater than 50%, while the gold nanorods and gold nanoshells had conversion efficiencies of 25% and 50%, respectively.¹⁶ Additionally, conductive polymer nanoparticles displayed higher photostability over several cycles of continuous laser irradiation in comparison to the behavior of gold nanoparticles. When compared to liposomes, polymeric nanoparticles were generally more stable and offered a more controllable drug-release profile.⁴³ They are also highly suitable for delivering hydrophobic drugs and for the co-encapsulation of multiple therapeutic agents against resistant cancer-cell lines.⁴³

In our laboratory, conductive polymer nanoparticles are prepared from the monomer 3,4-ethylenedioxythiophene (EDOT) using a two-surfactant oxidative-emulsion polymerization process. An aqueous phase and organic phase are prepared individually, with the surfactant poly(4-styrenesulfonic acid-co-maleic acid) sodium salt (PSS-co-MA)

used to prepare the aqueous phase, and dodecylbenzenesulfonic acid (DBSA) used with EDOT to prepare the organic phase, yielding poly(3,4-ethylenedioxythiophene) (PEDOT) NPs after an oxidative emulsion polymerization initiated by iron (III) chloride. Emulsion polymerization for the preparation of NPs is a process that is easily scalable, relatively fast, and is an effective method that yields NPs with a uniform colloidal morphology.¹⁵ In this work, the mechanisms by which these PEDOT nanoparticles mediate photothermal ablation of cancer cells was investigated.

1.2.4 Combination Therapy

Although chemotherapy is a frontline component of current cancer treatment, its effectiveness is extremely limited by the chronic damage and harmful side effects that may occur, which can range from nausea to cognitive dysfunction.⁴⁴ Many of these side effects occur because chemotherapy is systematically delivered and lacks specificity for tumor cells. Doxorubicin is a frontline chemotherapeutic drug for patients with a variety of cancer types, but cannot be utilized aggressively or for prolonged treatment because of the development of cardiotoxicity.⁴⁵ Combination therapy, which is the utilization of more than one therapeutic approach, has shown great potential for the treatment of cancer.⁴⁶ Apart from being directly utilized for photothermal ablation, the photothermal effects of NIR-absorbing nano-agents has also been exploited for controlled chemotherapeutic drug release, thus increasing the concentration of drug at the desired location. At the tumor level, nanoparticles act as a drug carrier able to target tumor tissue and protect the drug from undesired degradation during its transport.⁴³ The high surface

area of nanoparticles is advantageous for drug-loading, thus enhancing the drug's solubility, stability, and circulating half-lives.⁴⁷

Photothermal therapy in combination with chemotherapy can result in synergistic effects on tumor cells by promoting the accumulation of nontoxic doses of a drug in the targeted cells.⁴⁸ PEGylated liposomal doxorubicin called Doxil was the first nanomedicine to be approved by the US Food and Drug Administration and has had much success in clinical trials because of the reduced cardiotoxicity as compared to free doxorubicin.⁴⁹ Other traditional chemotherapy drugs have followed suit and have been encapsulated and delivered using similarly engineered nano-agents.⁴⁹ Shen et al. synthesized doxorubicin-loaded mesoporous silica-coated gold nanorods (DOX-pGNRs@mSiO₂) for drug delivery *in vivo* and observed a drug release profile that could be precisely controlled by pH and NIR light.⁵⁰ The DOX-pGNRs@mSiO₂ displayed a significantly faster drug release at pH 5.0 than at pH 7.4 and showed that the release of doxorubicin increased from 8.4% to 15.9% after 3 minutes of NIR irradiation at 3 W/cm²; the control did not indicate any such increase in drug release. For the *in vivo* study, the mice were randomized into 5 treatment groups: control group (1), laser only group (2), doxorubicin treated group (3), gold nanorods and laser group (4), and doxorubicin-loaded gold nanorods and laser group (5). Two hours after intravenous injection, the tumors were illuminated at 3 W/cm² for 30 seconds for groups 2, 4, and 5. The tumors in group 1 and 2 grew rapidly, whereas enhanced *in vivo* therapeutic effects were detected in group 2, 3, and 4 (Figure 2). Group 5 displayed the lowest tumor weights, with an inhibition rate of 66.5% compared to the control group. Compared with chemotherapy or photothermal therapy treatment alone, the combination of thermal heat and chemotherapy

in a single nano-agent showed a synergistic effect, resulting in higher *in vivo* therapeutic efficacy.⁵⁰ Gong et al. demonstrated that NIR-absorbing conjugated polymers could also be used for loading a variety of aromatic drug molecules, including doxorubicin, with high loading efficiencies.⁵¹ The PEDOT:PSS-PEG NPs were synthesized by being layer-by-layer coated with charged polymers and conjugated with branched polyethylene glycol (PEG).⁵¹ *In vitro* studies revealed a significant synergistic anticancer therapeutic effect when chemotherapy was combined with photothermal treatment. Additionally, PEDOT:PSS-PEG NPs exhibited a positive stimulation effect on

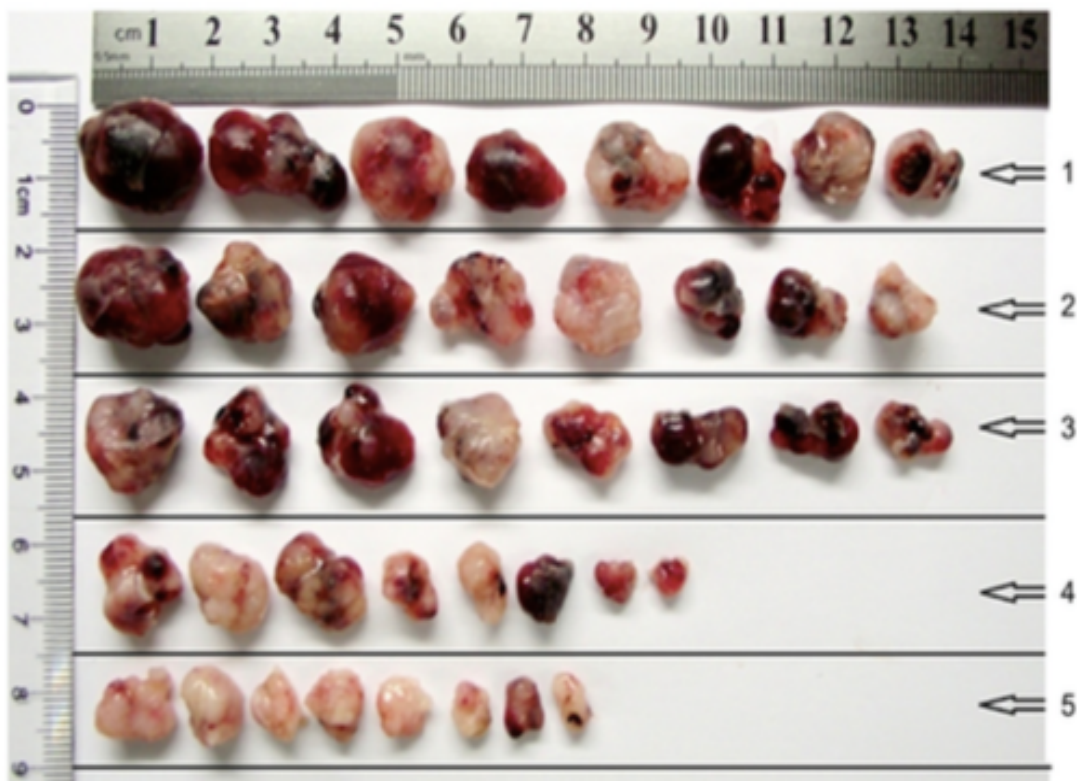


Figure 2. Targeting Silica-Encapsulated Gold Nanorods for Chemo-Photothermal Therapy. 808 nm NIR laser irradiation at 3 W/cm² with iv injected gold nanorods. Photograph of tumors after excision from (1) untreated group, (2) laser only group, (3) Free doxorubicin group, (4) gold nanorods with laser group, (5) Doxorubicin-loaded gold nanorods with laser group. Reference 50.

the immune system, specifically dendritic cells, which may show potential as a vaccine adjuvant.

1.2.5 Cell Death Mechanisms

Cell death is a crucial physiological process that regulates tissue homeostasis, development, and immune regulation of multicellular organisms by terminating normal cellular functions.⁵² Defects in cell-death pathways are associated with numerous pathologies, including cancer, autoimmunity, neurodegeneration, and infection.⁵³ A major characteristic of cancer is the failure to undergo apoptosis in response to inappropriate cell division, which can lead to uncontrolled cell growth and genomic instability.⁵⁴ The two most prominent cell death pathways include apoptosis and necrosis. Apoptosis is regarded as a programmed form of cell death that involves a cascade of energy-requiring molecular events that can be initiated by both external and internal factors, whereas necrosis is defined as premature injury-related cell death due to external stimuli that usually affects large populations of cells.⁵⁵ Distinct biochemical markers have been identified for the apoptotic pathway, but identification of necrotic cell death has little to rely on other than cellular morphology and the lack of apoptotic biochemical markers.⁵⁵

Necrosis is considered an adverse process where cell functions completely break down and the integrity of the plasma membrane ruptures, resulting in the leakage of intracellular constituents into the extracellular space and subsequent inflammation. The necrotic pathway is considered a passive process that lacks fundamental signaling events and occurs under extreme physicochemical conditions, such as abrupt anoxia, physical trauma, sudden shortage of nutrients, and exposure to detergents.⁵⁶ The morphological

changes of necrosis are characterized by cell swelling, formation of cytoplasmic vacuoles, disrupted organelle membranes, and disruption of the plasma membrane. Necrotic cell injury is mediated by either interference with the energy supply of the cell or direct damage to the cell's membrane. During the final stages of the necrotic pathway, the cells release pro-inflammatory factors from the cytoplasm including heat-shock proteins, histones, and cytokines.⁵⁶

Conversely, apoptosis involves a signaling pathway induced through intracellular signaling, extracellular receptors, and the mitochondria. Apoptosis occurs normally as part of the cell cycle during development to maintain cell populations, although it is inhibited in cancer cells to allow for dysregulated growth.⁵⁷ The two main apoptotic pathways are the extrinsic death receptor pathway and the intrinsic mitochondrial pathway. The extrinsic signaling pathway involves transmembrane receptor-mediated interactions, such as the FasL/FasR and TNF- α /TNFR1 models. The intrinsic pathway involves non-receptor mediated stimuli that produce intracellular signals that act directly on targets within the cell. These signals cause changes to the permeability of the outer mitochondrial membrane, releasing pro-apoptotic proteins, such as cytochrome c and endonuclease G, from the intermembrane space into the cytosol. The Bcl-2 family of proteins manages mitochondrial membrane permeability, ultimately controlling and regulating these apoptotic mitochondrial events.⁵⁷

An additional pathway also operates during T-cell mediated cytotoxicity and involves perforin-granzyme dependent killing of the cell.⁵⁷ T-cell mediated cytotoxicity is an alternative form of type IV hypersensitivity where signaled CD8 cells kill antigen-presenting cells. The cytotoxic T-lymphocytes are able to kill target cells via receptor-

mediated interactions that are part of the extrinsic pathway. The cytotoxic effects are exerted on tumor cells and virus-infected cells by a pathway that involves secretion of the transmembrane pore-forming molecule perforin, which causes a release of cytoplasmic granules through the pore and into the target cell for destruction.⁵⁸

The extrinsic, intrinsic, and granzyme pathways converge on the same terminal pathway, where the activation of execution caspases begins the phase of apoptosis.⁵⁹ Caspases are proteases that cleave target proteins only after an aspartic acid residue. Caspases are responsible for the degradation of hundreds of cytoplasmic and nuclear proteins that ultimately causes the disassembly of the apoptotic cell. Caspase-8, caspase-9, and caspase-10 act as initiator caspases, which are responsible for cleaving and activating the effector caspases. The effector, or “executioner”, caspases cleave various substrates that ultimately cause morphological and biochemical changes seen in apoptotic cells and include caspase-3, caspase-6, and caspase-7. Cleaved caspase-3 results in cell shrinkage, DNA fragmentation, degradation of nuclear proteins, formation of apoptotic bodies, expression of ligands for phagocytic cell receptors, and finally uptake by phagocytic cells such as macrophages. Once the cascade of proteolytic caspases is activated, the cell irreversibly commits towards cell death. Typically, apoptosis can be instigated by stress, heat, drugs, radiation, hypoxia, and viral infection. In contrast to necrosis, the integrity of the apoptotic cell membrane is preserved and the cell does not release its cellular constituents into the surrounding interstitial tissue, thus avoiding the production of anti-inflammatory cytokines.⁶⁰

Although the mechanisms and morphologies of apoptosis and necrosis differ, there is overlap between these two processes.⁶¹ Decrease in the availability of caspases

and intracellular ATP are two factors that will convert an ongoing apoptotic process into a necrotic process, a phenomenon described as the “apoptosis-necrosis continuum.” The two processes can occur simultaneously depending on the intensity and duration of the stimulus, the extent of ATP depletion, and the availability of caspases. Cultured cells undergoing apoptosis *in vitro* will eventually undergo secondary necrosis. Secondary necrotic cells resemble regular necrotic cells, but differ in having gone through an apoptotic stage. The time from initiation of apoptosis to completion can occur as quickly as 2-3 hours. Identifying apoptotic cells in culture can be difficult to do accurately, as each method available has advantages and disadvantages. A combination of these methods can give more accurate results on whether the apoptotic process is occurring in a cultured cell population.⁶²

There are numerous advantages to being able to control the induction of the apoptotic pathway in cancer cells in response to therapeutic approaches, with one of the most promising approaches being the blockade of immune checkpoints. While the immune system contains a number of inhibitory pathways that are critical in maintaining self-tolerance, it has recently been discovered that tumors also contain certain immune-checkpoint pathways that keep it resistant to the immune system, notably against T-cells that are specific for tumor antigens. By blocking ligand-receptor interactions at immune-checkpoints through the use of antibodies or other forms of ligands, the immune system would be able to identify and eliminate tumor cells, which is the basis of checkpoint-blockade immunotherapy. Cancer cell apoptosis mediated by localized photothermal therapy is believed to better initiate an immune response toward the cancer cells, leading to a systemic immune attack of primary and metastatic tumors by anti-cytotoxic T-

lymphocytes.³ This therapeutic strategy combining adjuvant nanoparticle-based PTT with checkpoint-blockade immunotherapy shows vaccine-like functions that offer a strong immunological memory effect, providing protection against tumor rechallenge (i.e. the implantation of a new set of cancer cells) after elimination of their initial tumors.³ Although the mode of cell death induced by PTT can be tuned between apoptosis or necrosis by alternating photothermal agent dose and irradiation parameters, low dose PTT/mild hyperthermia has been shown to favor apoptosis.⁶³ A preliminary clinical study was conducted to evaluate the safety and therapeutic efficacy of *in situ* photoimmunotherapy (ISPI) for the treatment of late-stage metastatic melanoma. ISPI consisted of local application of imiquimod to multiple cutaneous metastases, injection of indocyanine green (ICG), and an 805 nm laser for local irradiation. ICG was used as the photothermal agent that absorbed the NIR radiation and dissipated it back as heat, while the imiquimod (a toll-like receptor agonist) was selected as the immunoadjuvant based on its strong immunological stimulating effect. The absence of grade 4 toxicity, minimal side effects, promising patient response rate, and 12-month overall survival rate of 70% indicated that *in situ* photoimmunotherapy with imiquimod is safe and well tolerated.⁶⁴

Our work aimed to identify and evaluate the mechanisms of cell death caused by photothermal ablation in order to optimize the parameters surrounding photothermal therapy mediated by conductive polymer nanoparticles.

Chapter II

MATERIALS AND METHODS

2.1 Materials

3,4-Ethylenedioxythiophene (EDOT), poly(4-styrenesulfonic acid-co-maleic acid) (PSS-co-MA) sodium salt (20,000 Da, 3:1 styrenesulfonic acid:maleic acid), and bovine serum albumin (BSA) were purchased from Sigma-Aldrich (St Louis, MO, USA). 4-dodecylbenzenesulfonic acid (DBSA) was purchased from TCI America (Portland, OR, USA). Nile Red was bought from Chem-Impex International, Inc (Wood Dale, IL, USA). One hundred kilo Dalton molecular weight cutoff cellulose ester membranes were obtained from Spectrum Laboratories (Rancho Dominguez, CA, USA). Triton X-100 was purchased from JT Baker, Inc (Phillipsburg, NJ, USA). Rabbit anti-alpha tubulin monoclonal antibody (stock concentration: 0.166 mg/mL, product number: ab176560) and goat anti-rabbit IgG Dylight 488 polyclonal antibody (stock concentration: 0.5 mg/mL, product number: ab96883) were purchased from Abcam (Cambridge, MA, USA). Glycerol, gelatin, and 4',6-diamidino-2-phenylindole, dihydrochloride (DAPI) were obtained from MilliporeSigma (Burlington, MA, USA). Fluoromount-G was bought from Southern Biotech (Birmingham, AL, USA). Ultrapure deionized water (DI water) was obtained from a Millipore Direct-Q water purification system.

2.2 Monomer Purification

3,4-ethylenedioxythiophene was decanted into dichloromethane. The solution was then extracted with 0.1 M HCl, using equal part of HCl to dichloromethane, using a

separatory funnel under a fume hood. The mixture was then washed with saturated sodium bicarbonate until the wash is neutral. DI water was used for the sodium bicarbonate wash and mixed with EDOT solution. After 3 or 4 washes, pH paper was used to confirm the solution was neutral and then dried over magnesium sulfate. The solution was then filtered through silica using vacuum filtration and filter paper. The methylene chloride was removed under reduced pressure. Initially, the pressure was reduced slowly, making sure that condensation was occurring in the bulb. If there was no condensation, the pressure was reduced more until it eventually hit ~10 mbar. The EDOT was then distilled under vacuum at 90°C at 0.65 torr. Once distillation was finished, the purified product was stored in the dark at -25°C under argon.

2.3 Synthesis of poly(3,4-ethylenedioxythiophene) (PEDOT) NPs

Conductive polymer nanoparticles were prepared from the monomer 3,4-ethylenedioxythiophene (EDOT) using a two-surfactant oxidative-emulsion polymerization process similar to that reported by Cantu et al (Figure 3).¹⁶ An aqueous phase and organic phase were prepared individually. For the aqueous phase, the surfactant poly(4-styrenesulfonic acid-co-maleic acid) (PSS-co-MA) sodium salt was dissolved in 1 mL of ultrapure water at a concentration of 2% w/v. The organic phase was prepared by making a solution consisting of a 48 mg/mL concentration of EDOT and a 0.3 g/mL concentration of the second surfactant 4-dodecylbenzenesulfonic acid (DBSA) in 100 μ L of chloroform. The organic phase was added dropwise to the aqueous phase in 10 μ L intervals while stirring, and then diluted with 2 mL of ultrapure water. Finally, 3.8 μ L of a 100 mg/mL aqueous solution of FeCl₃ (2.2 mol) was added to the

emulsion and allowed to polymerize for 1 hour while stirring. The nanoparticles were allowed to dialyze overnight for 17 hours using a 100-kDa molecular weight cutoff cellulose ester membrane.

PEDOT NPs physically encapsulating Nile Red (PEDOT/NR) were synthesized in order to visually monitor the cellular uptake of the NPs by breast cancer cells, and were prepared using the same two-surfactant oxidative emulsion polymerization process. 100 μL of a 4 mM solution of Nile Red in toluene was prepared and directly added to EDOT and DBSA to form the organic phase. The organic phase was added to the aqueous phase in the same dropwise fashion. After the addition of the FeCl_3 and 1-hour polymerization period, the PEDOT/NR NPs were dialyzed overnight.

The concentration of NPs was determined by weighing the lyophilized product from 1 mL of the NP suspension.

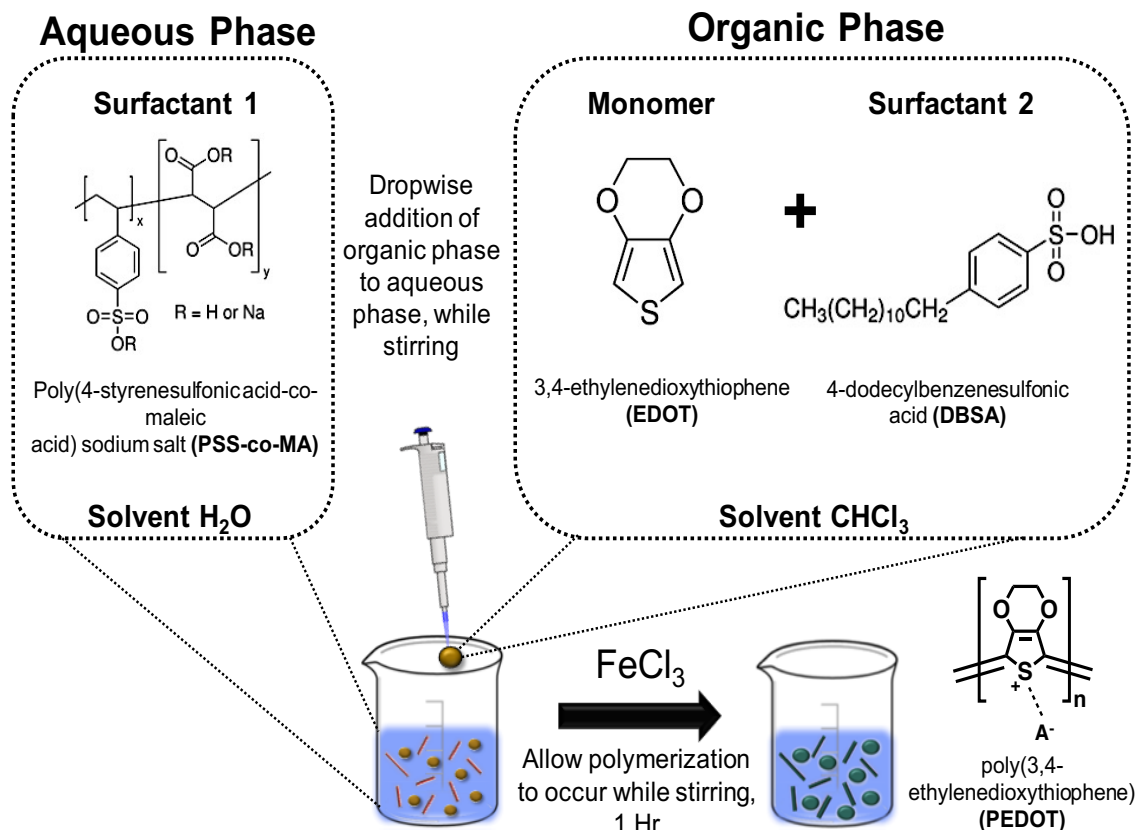


Figure 3. Schematic of PEDOT NP Preparation. Organic phase is added to the aqueous phase in dropwise intervals while stirring to create an emulsion. FeCl₃ is added to the emulsion, yielding PEDOT NPs. A⁻ in the chemical structure represents the negatively charged surfactants (anions) interacting with the positively charged polymer.

2.4 Characterization of PEDOT NPs

UV/VIS/NIR absorption spectroscopy was used to confirm strong absorption of the PEDOT nanoparticles in the NIR region using a Biotek Synergy H4 Hybrid Multi-Mode Microplate Reader. Dynamic light scattering and zeta potential analysis were performed to validate the size and zeta potential of the nanoparticles using a Malvern Zetasizer Nano ZS instrument. For size determination, 1 mL of the stock NP suspension was added to a cuvette and analyzed. For zeta potential analysis, 3-4 drops of the NP

suspension was added to 1 mL of 1 mM KCl solution. Scanning electron microscopy (SEM) was used to confirm the size and shape of the nanoparticles. SEM samples were prepared by drop casting the NP suspension onto a Si wafer, coated with 2 nm of iridium using an EMS150T ES sputter coater, and imaged using an FEI Helios NanoLab 400 SEM at a working distance of 4 mm and at 10 kV.

2.5 Effect of PEDOT NPs on Laser-Induced PTT

Adequate temperature change as a function of nanoparticle concentration and laser irradiation time in the absence of cells was verified for the photothermal ablation agents using an 808-nm laser diode (RLCO-808-1000G, 9 mm; Roithner Lasertechnik GmbH, Wein, Austria) rated at 1 W of power and a thermocouple. A biconvex lens (Thorlabs, Inc., Newton, NJ, USA) was used to focus the laser to a 6 mm diameter, which was mounted at $\sim 25^{\circ}\text{C}$. A VIS/NIR detector card (400 to 640 nm, 800 to 1700 nm, Thorlabs, Inc., Newton, NJ, USA) that converts NIR light to visible light was used to visualize the laser beam and confirm the size of the diameter of the laser beam. All samples were irradiated at a laser power of 0.85 W (3.0 W/cm^2) in 96 well plates that were placed 8 cm below the biconvex lens. Power intensity was measured using a photometer. PEDOT NP suspensions were diluted with DPBS to 10, 50, 100, and 500 $\mu\text{g/ml}$ concentrations, and irradiated for 1, 5, and 15 minutes each. The thermocouple was used before and after each irradiation cycle to assess the temperature change due to the nanoparticles. Controls that lacked nanoparticles and consisted of only DPBS were also irradiated with the NIR laser. Each tested sample was performed in triplicate.

2.6 Cell Culture

Human MDA-MB-231 breast cancer cells (American Type Culture Collection, Manassas, VA, USA) were seeded in T-75 flasks with cell media consisting of 88% Dulbecco's Modified Eagle's Medium (DMEM, Corning Cellgro, Corning, NY, USA), 10% Fetal Bovine Serum (FBS, Corning Cellgro, Corning, NY, USA), 1% 4-(2-hydroxyethyl)-1-piperazineethanesulfonic acid (HEPES, ThermoScientific, Waltham, MA, USA), and 1% Penicillin Streptomycin solution (Sigma, St. Louis, MO, USA) at 37°C with 5% CO₂. Once cells reached 80% confluency, cells were dissociated using 0.05% trypsin-EDTA solution and centrifuged at 62 RCF for 5 minutes. For confocal imaging, cells were seeded at 50,000 cells/well in 12-well plates that contained a single autoclaved circular coverslip in each well. For nanoparticle-mediated photothermal therapy, cells were seeded in 96-well plates at a sample volume of 100 μ L and a cell density of 20,000 cells/well. Cells were incubated for 24 hours prior to experimentation in order to enable the cellular adhesion process. NPs were filtered with a sterile 0.22 μ m polyethersulfone membrane filter before being introduced to the cells. All PTT studies were performed in an adjusted incubator environment in order to mimic the optimal temperature setting for the cell line, which is 37°C. This was done to verify that the cells were dying solely by the PTT and not because they were being subject to sub-optimal growing conditions.

2.7 Cell Internalization

To observe whether the PEDOT NPs were being internalized into the MDA-MB-231 cancer cells, cells were grown, fixed, and fluorescently stained on glass coverslips. A

sterilized circular coverslip was treated with a filtered 0.1% gelatin-coating solution in the well of a 12 well plate to aid in the cell adhesion process. The coverslip was incubated in the gelatin solution for 10 minutes at room temperature and allowed to dry for 15 minutes before use. The gelatin-treated coverslip was placed in a new well and seeded with 50,000 cells/well. After 24 hours, 1 mL of 500 $\mu\text{g/ml}$ PEDOT/NR NPs was introduced to the cells and allowed to incubate for 1.5 and 24-hour time periods. After the respective incubation time, the cells were washed with cold DPBS, fixed with 4% paraformaldehyde for 20 minutes at room temperature, and washed with 0.1% BSA in 1X PBS twice. Blocking buffer containing 1% BSA, 0.1% Triton X-100, and 22.5 mg/mL glycerol was added to the well and incubated for 45 minutes at room temperature. The primary anti-alpha tubulin antibody was introduced in a 1:200 dilution and allowed to incubate for an hour at room temperature. The cells were washed twice with 0.1% BSA in 1X PBS, followed by the addition of a 1:1000 dilution of the fluorescently labeled secondary goat anti-rabbit IgG Dylight 488 antibody that was incubated for 1 hour at room temperature in the dark. After rinsing twice with wash buffer, a 1 $\mu\text{g/ml}$ solution of DAPI was added to the well for 5 minutes and then rinsed with DI water. The coverslip was carefully removed from the well, inverted onto a slide containing 500 μl of Fluoromount-G, and secured using clear nail polish. The slide was immediately viewed and analyzed using an Olympus FluoView™ FV1000 laser scanning confocal microscope.

2.8 Photothermal Effect on Cell Death

Cell death was qualitatively analyzed by fluorescence microscopy using Calcein Blue AM, Annexin V AlexaFluor 488, and Propidium Iodide as biochemical indicators of live, apoptotic, and necrotic cells, respectively. Calcein Blue AM labels live cells that display enzymatic activity with blue fluorescence. Annexin V AlexaFluor 488 labels apoptotic cells by detecting translocated phosphatidylserine that is exposed on the plasma membrane of early apoptotic cells, which is indicated by green fluorescence. Propidium iodide is a nucleic acid stain that detects necrosis by being able to permeate through the compromised plasma membrane of necrotic cells, and is indicated by red fluorescence. Figure 4 shows the absorption and fluorescence spectra of these three fluorescent biochemical indicators. As shown, little to no spectral overlap occurs in the fluorescence of these fluorophores. Additionally, Table 1 displays the excitation and emission wavelengths of the fluorescently labeled biochemical reagents along with their compatible filter cubes.

Following the 24-hour incubation period after cell seeding, the media was replaced with filtered NPs diluted with cell media without phenol red at NP concentrations of 10, 50, 100, and 500 $\mu\text{g}/\text{ml}$. The cancer cells were exposed to 100 μL of NPs for 1.5, 6, 12, and 24-hour incubation time periods, and irradiated in the presence of the NPs. Cells were irradiated for 1, 5, and 15 minutes using an 808-nm laser diode (RLCO-808-1000G, 9 mm; Roithner Lasertechnik GmbH, Wein, Austria) at 3.0 W/cm^2 . Following treatment with the laser, cells were incubated for an additional 30 minutes at 37°C with 5% CO_2 before the addition of fluorescently labeled biochemical reagents and imaging to allow for the cellular processes to take place.

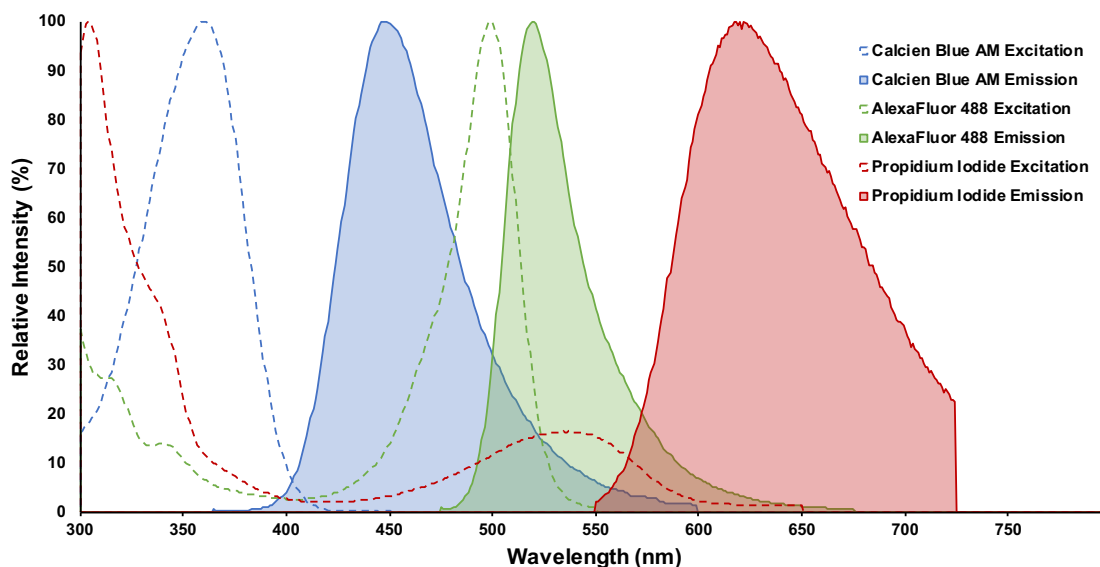


Figure 4. Excitation and Emission Spectra of Calcein Blue AM, AlexaFluor488, and Propidium Iodide

Table 1. Excitation and Emission Wavelengths of the Fluorescently Labeled Biochemical Reagents and Compatible Filter Cubes

Fluorophore	Ex (nm)	Em (nm)	Compatible Light Cube	Ex (nm)	Em (nm)
Calcein Blue AM	360	449	DAPI	357±22	447±30
AlexaFluor488	488	499	GFP	470±21	510±21
Propidium Iodide	535	617	RFP	531±20	593±20
CellEvent™ Reagent	503	530	GFP	470±21	510±21

Positive and negative controls consisted of live cells without any treatment, induced necrotic cells treated with methanol for 10 minutes, induced apoptotic cells using UV radiation for 1-hour, live cells exposed to laser irradiation for the same times used for all samples but without nanoparticles, and live cells exposed to all nanoparticle concentrations without irradiation. Control studies were performed in order to help

distinguish the morphological and biochemical differences between the two most common types of cell death, apoptosis and necrosis.

Before use, Calcein Blue AM was diluted with DPBS to 10 μM working solution. The Annexin Binding Buffer that was utilized to enhance the binding of annexin to phosphatidylserine was composed of 50 mM HEPES, 700 mM NaCl, and 12.5 mM CaCl_2 at a pH of 7.4. 100 μL of the Calcein Blue AM solution, 25 μL of 1x Annexin Binding Buffer, 4 μL of Annexin V AlexaFluor 488, and 2 μL of 100 $\mu\text{g}/\text{mL}$ Propidium Iodide were added to each well, allowed to incubate at room temperature for 15 minutes, and imaged using an EVOS FL optical microscope. Table 1 lists the excitation and emission peaks for each of the fluorescence indicators used and the light cubes utilized for viewing the samples on the EVOS FL microscope.

2.9 Photothermal Effect on Caspase-3/7 Expression

Activation of caspase-3 is an essential event during apoptosis. Thus, caspase expression was analyzed by fluorescence microscopy using CellEvent™ Caspase-3/7 Green Detection Reagent (ThermoFisher Scientific, Waltham, MA, USA) in order to confirm apoptotic cells. This reagent is an amino acid peptide (DEVD) that is conjugated to a nucleic acid-binding dye. Activated caspase 3/7 cleaves at the DEVD peptide sequence, which allows the conjugated dye to bind to DNA and fluoresce green. Caspase-3/7 studies were set up similarly to the previous PTT experiments and tested for the same experimental variables. After the samples underwent PTT and the 30-minute incubation period at 37°C with 5% CO_2 , the NP-media was removed and replaced with 100 μL of 5 μM CellEvent Caspase-3/7 Green Detection Reagent. Before use, the CellEvent Caspase-

3/7 Green Detection Reagent was diluted with DPBS to a 5 μ M working solution.

Samples were allowed to incubate for an additional 30 minutes before analysis, and then imaged using the GFP filter cube on an EVOS FL optical microscope (Table 1).

2.10 Image Quantification

Fluorescence intensity quantification of microscopy images was performed using ImageJ software. Colored images (RGB) were first converted to 16-bit grayscale, duplicated, and then used to create a binary image. A range of pixel intensities were chosen, with the lower threshold level set to 15 and the upper threshold level set to 200 for all images. The pixel intensities were analyzed and compared to the background fluorescence. The following equation was used to calculate the Corrected Total Cell Fluorescence (CTCF):

$$\text{(Eq. 1)} \quad \text{CTCF} = \text{Total Integrated Density of Cells} - (\text{Area of Selected Cells} \times \text{Mean Fluorescence of Background Readings})$$

2.11 Flow Cytometry

Flow cytometry is a common laser-based technology that is capable of analyzing characteristics of cells or particles, such as cell size or fluorescence intensity. Cell suspensions are passed through a laser beam in a single-file fashion, where the resulting scattered light is detected and measured as forward scatter and side scatter. Fluorescence detectors also measure the amount of emitted fluorescence from positively stained cells.

To quantitatively analyze the cell death pathways by flow cytometry, cells were stained using Annexin V AlexaFluor488 and Propidium Iodide in order to determine the proportion of apoptotic and necrotic events within a cell population that had underwent

nanoparticle-mediated photothermal therapy. Cells that were Annexin V AlexaFluor488 positive but PI negative were considered to have undergone apoptosis. Cells which were positive for both Annexin V AlexaFluor488 and PI were considered to have undergone necrosis. Cell cultures were plated overnight and nanoparticles were introduced the following day and allowed to incubate for their designated time period. Following PTT, the samples were incubated for an additional 30 minutes. Briefly, the cells were washed, trypsinized, and centrifuged at 62 RCF for 5 minutes in microcentrifuge tubes. The supernatant was discarded and the cell pellets were resuspended in 100 μ L of Annexin Binding Buffer containing 3 μ L Annexin V AlexaFluor488 and 1 μ L PI. Each sample was mixed by gentle pipetting and incubated for 15 minutes at room temperature in the dark. As a control, live cells that were not exposed to NPs or irradiation were stained (negative control), as well as cells exposed to 1 hour of UV radiation (apoptotic positive control) and cells exposed to 10 minutes of methanol (necrotic positive control). Samples were placed on ice until analysis using a BD Accuri C6 Flow Cytometer with bandpass filters at 533 ± 15 for Annexin V AlexaFluor488 and >670 for PI. A total of 20,000 events were collected for each sample. FlowJo software was used to analyze and process flow cytometry data into log-log pseudocolor density plots. Gating, or the selection of fluorescence levels that separate live, apoptotic, and necrotic cells, was determined based on the distinct populations and relative fluorescence demonstrated by the live, apoptotic, and necrotic control samples. Upon gating, the relative percentage of cell population in each treated sample that was live, apoptotic, or necrotic was determined.

2.12 Statistical Analysis

Unpaired t-tests were used to determine statistical significance between the means of independent sample conditions. Values of $P < 0.05$ were utilized to categorize statistical significance.

Chapter III

RESULTS

3.1 PEDOT and PEDOT/NR NP Characterization

The oxidative emulsion polymerization process yielded a dark green PEDOT NP suspension after the addition of the oxidizer FeCl_3 , as seen in Figure 5A. Despite using the same protocol for the synthesis of the PEDOT/NR NPs, the color of both the emulsion and the suspension differed from that of the PEDOT NPs lacking the Nile Red dye, and yielded a lighter green suspension (Figure 5D). UV/VIS/NIR spectroscopy displayed a strong absorbance in the NIR region (700–1000nm) for the PEDOT NPs, with a peak absorbance at 790 nm (Figure 6A). NIR radiation is able to penetrate deep within tissue without being absorbed by biological chromophores such as hemoglobin,

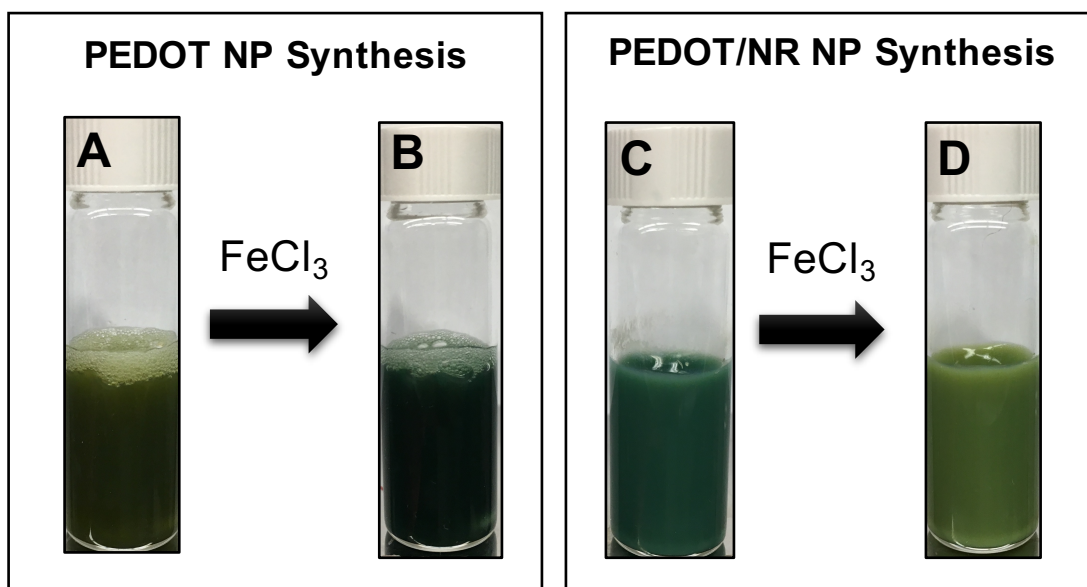


Figure 5. PEDOT and PEDOT/NR NP Synthesis. (A) Oil-in-water emulsion before addition of the oxidizer FeCl_3 . (B) PEDOT NP suspension after addition of FeCl_3 . (C) Oil-in-water emulsion in the presence of Nile Red before addition of the oxidizer FeCl_3 . (D) PEDOT/NR NP suspension after addition of FeCl_3 .

which makes the PEDOT NPs a prime candidate for photothermal therapy. PEDOT NPs exhibited a spherical morphology as displayed in the SEM images, with an average diameter of 71.49 nm confirmed by dynamic light scattering and a polydispersity index (PDI) of 0.261. PDI refers to the size heterogeneity of the particles in suspension and is calculated by dividing the mean size of the NPs by the standard deviation. A more polydispersed suspension generally has a $PDI > 0.6$, while a monodispersed suspension has a PDI close to 0. Zeta potential analysis revealed that the NPs are roughly -30 mV (Figure 6). Table 2 summarizes the sizes and zeta potentials for the particles. The <100 nm agents are within the optimal size range for utilization within a living organism, where they should be small enough to evade the security of the immune system, but large enough to not be easily cleared by the renal system.

The characterization of the PEDOT/NR NPs yielded very similar results, with an average size of 62.64 nm, a PDI of 0.274, and a zeta potential of -40.8 mV. Since we are assuming the PEDOT NPs are being internalized by the cells in a similar fashion as the PEDOT/NR NPs, it is crucial that the encapsulation of the Nile Red dye does not have a significant impact on the conductive properties, size, or zeta potential of the nanoparticles and the data confirms this.

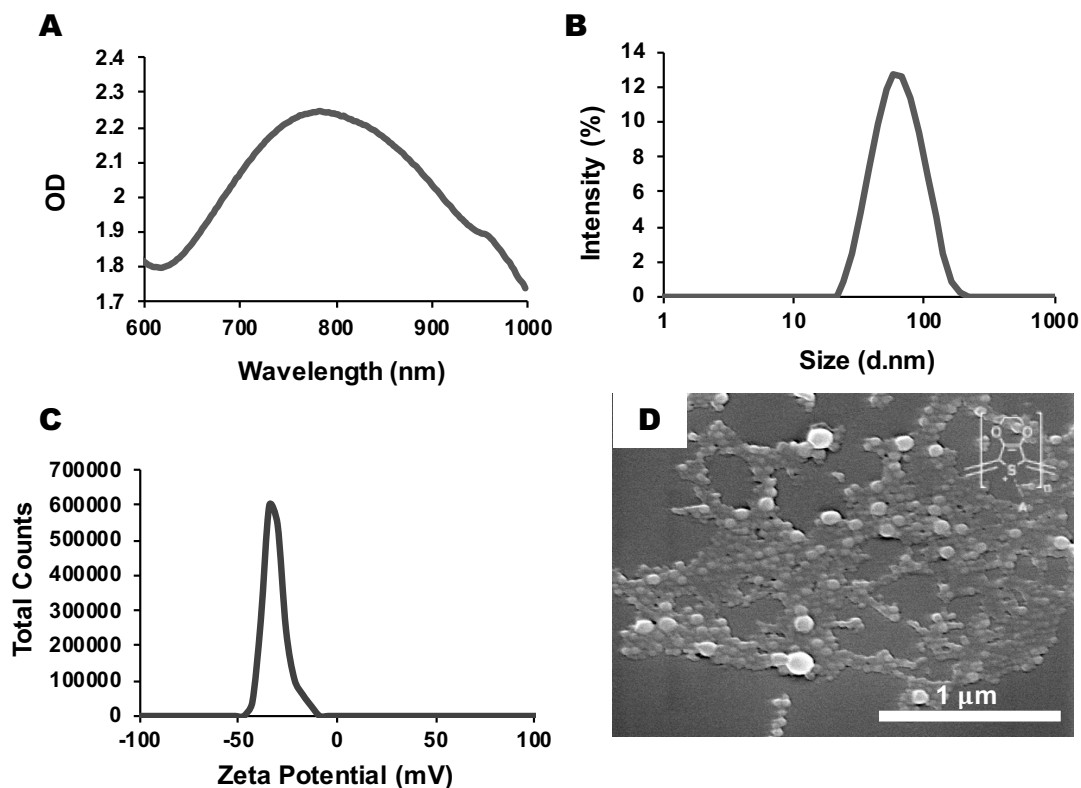


Figure 6. PEDOT NP Characterization. (A) Absorbance spectrum of PEDOT NPs in the NIR region; peak absorbance at 790 nm. (B) Dynamic light scattering displayed average PEDOT NP size to be 71.49 nm. (C) Zeta potential analysis indicated PEDOT NPs to have an average zeta potential of -30.9 mV. (D) Scanning electron microscopy (SEM) confirmed NP size was <100 nm.

Table 2. Size, PDI, and Zeta Potential of PEDOT and PEDOT/NR NPs. Standard deviations were calculated from 3 different batches of NPs. P-values were calculated using an unpaired t-test (*P > 0.05) by comparing the PEDOT and PEDOT/NR NPs based on size, PDI, and zeta potential.

	Size (nm)*	PDI*	Zeta Potential (mV)*
PEDOT NPs	71.49 ± 7.29	0.261 ± 0.029	-30.9 ± 5.9
PEDOT/NR NPs	62.64 ± 8.73	0.274 ± 0.027	-40.8 ± 6.3
P-value	0.2490	0.6002	0.1179

3.2 Photothermal Effect of PEDOT NPs

The change in temperature upon laser irradiation as a function of PEDOT NP concentrations is displayed in Figure 7. The temperature increase of 500 $\mu\text{g/ml}$ NP suspensions after 1, 5, and 15 minutes of irradiation using a NIR laser at 3.0 W/cm^2 was 16.9, 26.5, and 30.8 $^\circ\text{C}$, respectively. Measuring the increase in temperature from the physiological temperature of 37°C , the maximum increase in temperature for the 500 $\mu\text{g/ml}$ concentration after 15 minutes of irradiation was almost 70°C . As previously observed in our published work, the change in temperature with respect to laser irradiation time stops increasing after approximately 5 to 6 minutes of irradiation, where the heat input of the system equals the heat output of the surrounding, reaching steady state, and accounting for the very minimal change in temperature between the 5 and 15-minute NP irradiation periods seen in Figure 7. Regression indicated a linear relationship between NP concentration and temperature change as demonstrated with R^2 values greater than 0.97 for the best-fit trendline of all nanoparticle concentrations when irradiated for the same time period, (Table 3), as expected. When samples lacked NPs, there was no change in temperature after 15 minutes of irradiation as measured with the thermocouple.

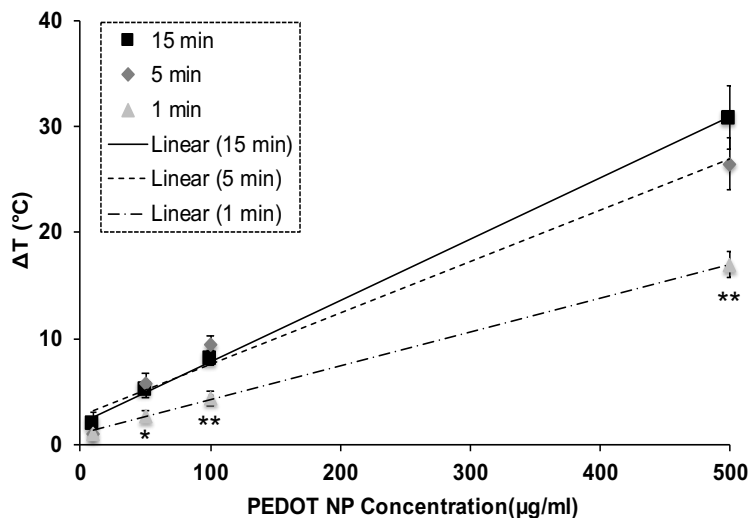


Figure 7. Temperature change (°C) as a function of NP concentration ($\mu\text{g/ml}$) after 1, 5, and 15 minutes of irradiation using an 808-nm laser at 3.0 W/cm^2 . Experiments were performed in triplicate. P-values were calculated using an unpaired t-test (** $P < 0.0025$, * $P < 0.025$) by comparing the 1 and 5 min irradiation times to the 15 min irradiation time.

Table 3. R^2 values for each irradiation time period. All R^2 values are > 0.95 , indicating there is a direct and linear relationship between NP concentration (10, 50, 100, and 500 $\mu\text{g/ml}$) and temperature change (°C).

Irradiation Time (min)	R^2 value
1	0.9989
5	0.9762
15	0.9989

3.3 Cellular Internalization of PEDOT NPs

Although conductive polymers are known to naturally fluoresce, our PEDOT NPs did not display adequate fluorescence at any point in the spectrum when tested at various excitation wavelengths (Appendix Figure A1), where the NPs were excited in 10 nm increments ranging from 300-450 nm. A peak fluorescence of ~ 70 RFU was seen at 400 nm after exciting at 360 nm. However, the fluorescence intensity of the NPs was not high enough to be detected with an EVOS microscope using the DAPI filter (Ex: 357/44, Em: 447/60). The encapsulation of Nile Red within the PEDOT NPs provided a much higher fluorescence intensity that could be easily detected with an EVOS microscope using the RFP filter (Ex: 531/40, Em: 593/40). As shown in Appendix Figure 2, a peak fluorescence value of ~ 1200 RFU was observed at 650 nm for the PEDOT/NR NPs

synthesized with toluene after being excited at 530 nm, while the PEDOT NPs displayed no fluorescence when excited at this same wavelength. Therefore, the high fluorescence intensity exhibited by the encapsulated Nile Red was utilized to study the internalization of the PEDOT NPs within the breast cancer cells.

The cellular uptake and distribution of Nile Red-loaded PEDOT NPs in breast cancer cells was observed with a confocal microscope after 1.5 and 24-hour co-incubation time periods (Figure 8). After 1.5 hours, the NPs (red fluorescence in Figures 8 C and D) appeared to enter the cells through endocytosis at the plasma membrane as a result of our observation of the red fluorescent vesicles which appeared to be endosomes. As expected, there seemed to be little to no penetration of the NPs into the nucleus. After 24 hours of co-incubation, the NPs had travelled from the plasma membrane to the perinuclear region, with still no penetration into the nucleus (Figure 8D). There was a much larger accumulation of NPs within the cytoplasm and an increase in number of NPs surrounding the nuclei of the cells. The nature of the NPs to travel to the perinuclear region and accumulate around the nucleus demonstrates their potential, not only as photothermal agents, but also as a drug delivery agent that could transport and deliver chemotherapeutic drugs to the nuclei of target tumor cells, where they can carry out their desired therapeutic effect.

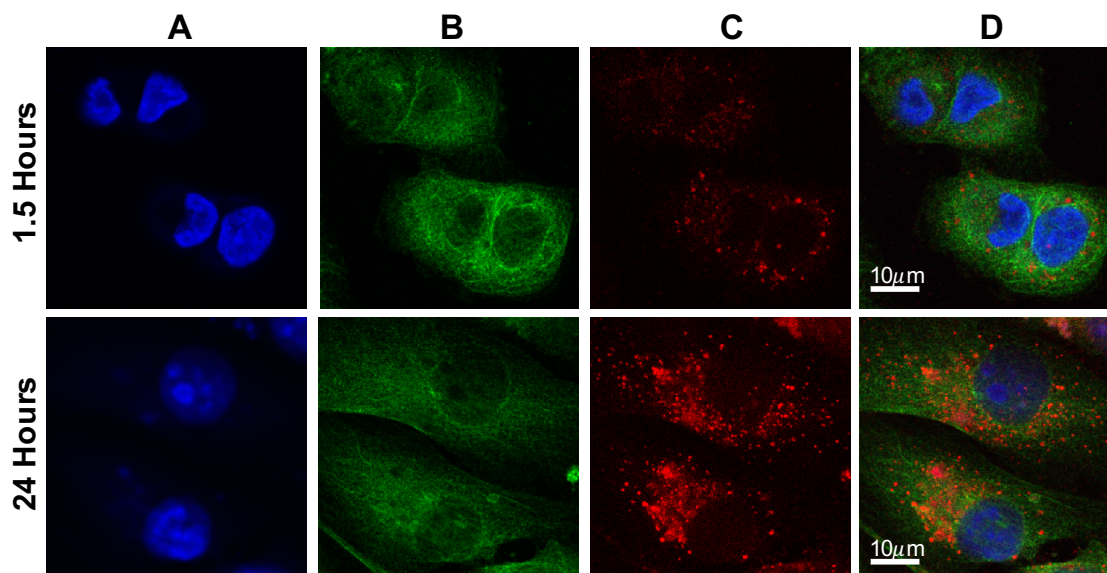


Figure 8. Confocal microscopy images of MDA-MB-231 cells co-incubated with 500 $\mu\text{g/ml}$ concentrations of PEDOT/NR NPs for 1.5 and 24-hour time periods. (A) Nucleus stain DAPI, (B) Tubulin, (C) Nile Red, (D) Overlay.

3.4 Qualitative Analysis of Cell Death by Fluorescence Microscopy

Using the fluorescently labeled biochemical indicators explained in Figure 4, cell death was qualitatively analyzed as a function of nanoparticle concentration, laser irradiation time, and NP-cell incubation time using fluorescence microscopy. Figure 9 displays the results of the fluorescence microscopy control studies. The negative control containing live cells without any treatment fluoresced blue from the Calcein Blue AM, as well as the irradiated control that was exposed to 15 minutes of irradiation without NPs. The blue fluorescence from the irradiated control suggests that the NIR radiation is not harmful to the cells by itself at the tested irradiation time. Additionally, the positive necrotic control that was exposed to 10 minutes of MeOH displayed bright red fluorescence from PI. The positive apoptotic control that was exposed to 1 hour of UV

radiation showed mostly green fluorescence as an indicator of apoptosis from Annexin V AlexaFluor488.

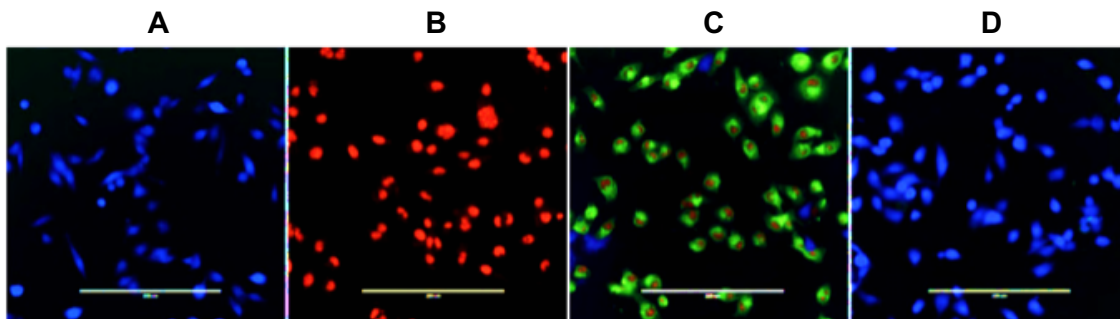


Figure 9. Fluorescence Microscopy Images of Control Samples. (A) Live cells without any treatment (negative control). (B) Cells treated with MeOH for 10 minutes (positive necrotic control). (C) Cells Exposed to UV radiation for 1 hour (positive apoptotic control). (D) Cells exposed to NIR radiation for 15 minutes Without the presence of NPs (irradiated control). Scale bar = 200 μm .

As seen in Figures 10-13, MDA-MB-231 breast cancer cells exposed to NPs at 10 $\mu\text{g/ml}$ and 50 $\mu\text{g/ml}$ displayed fluorescence by mostly Calcein Blue, indicating that they were alive and metabolically active regardless of the NP-cell incubation period and/or irradiation time. However, complete cell death was seen for the 500 $\mu\text{g/ml}$ concentration at every NP-cell incubation time period after 5 and 15 minutes of irradiation, indicated by the complete lack of blue fluorescence. After 1.5 hours of NP incubation and 15 minutes of irradiation, the 50 $\mu\text{g/ml}$ NP concentration began to initiate an observable cellular response by the Annexin V AlexaFluor488 green fluorescence, which was the more prominent fluorescent biochemical marker for the indication of apoptosis (Figure 10). The 100 and 500 $\mu\text{g/ml}$ NP concentrations after the 1.5-hour incubation period continued to activate this cell death pathway, with a significant increase in cell death by apoptosis as indicated by the Annexin V marker as the irradiation time increased. Breast cancer cells that were not irradiated with the NIR laser (0 minutes) but exposed to 10, 50, 100,

and 500 $\mu\text{g/ml}$ NP concentrations displayed blue fluorescence, indicating that the cells were alive and the NPs were not toxic at the tested concentrations/ NP exposure times. After 6 hours of incubation with the NPs, the red fluorescence indicative of PI was much more visible in the 100 and 500 $\mu\text{g/ml}$ concentration after 15 minutes of irradiation, signifying higher levels of cellular ablation leading to cell necrosis (Figure 11). Total cell death appeared to occur after only 1 minute of irradiation at the 500 $\mu\text{g/ml}$ concentration. The results from the 12-hour incubation period appeared visually similar to the 6-hour incubation, with the red fluorescence from the PI being the more distinct biomarker at all irradiation times for the 500 $\mu\text{g/ml}$ concentration (Figure 12). Furthermore, the 24-hour incubation period conveyed cellular necrosis as the favored cell death pathway by the almost complete lack of green and blue fluorescence, even after just 1 minute of irradiation (Figure 13). After 24 hours of NP exposure without irradiation, the cells still displayed prominent blue fluorescence at every concentration, indicating their potential as cytocompatible, photothermal agents.

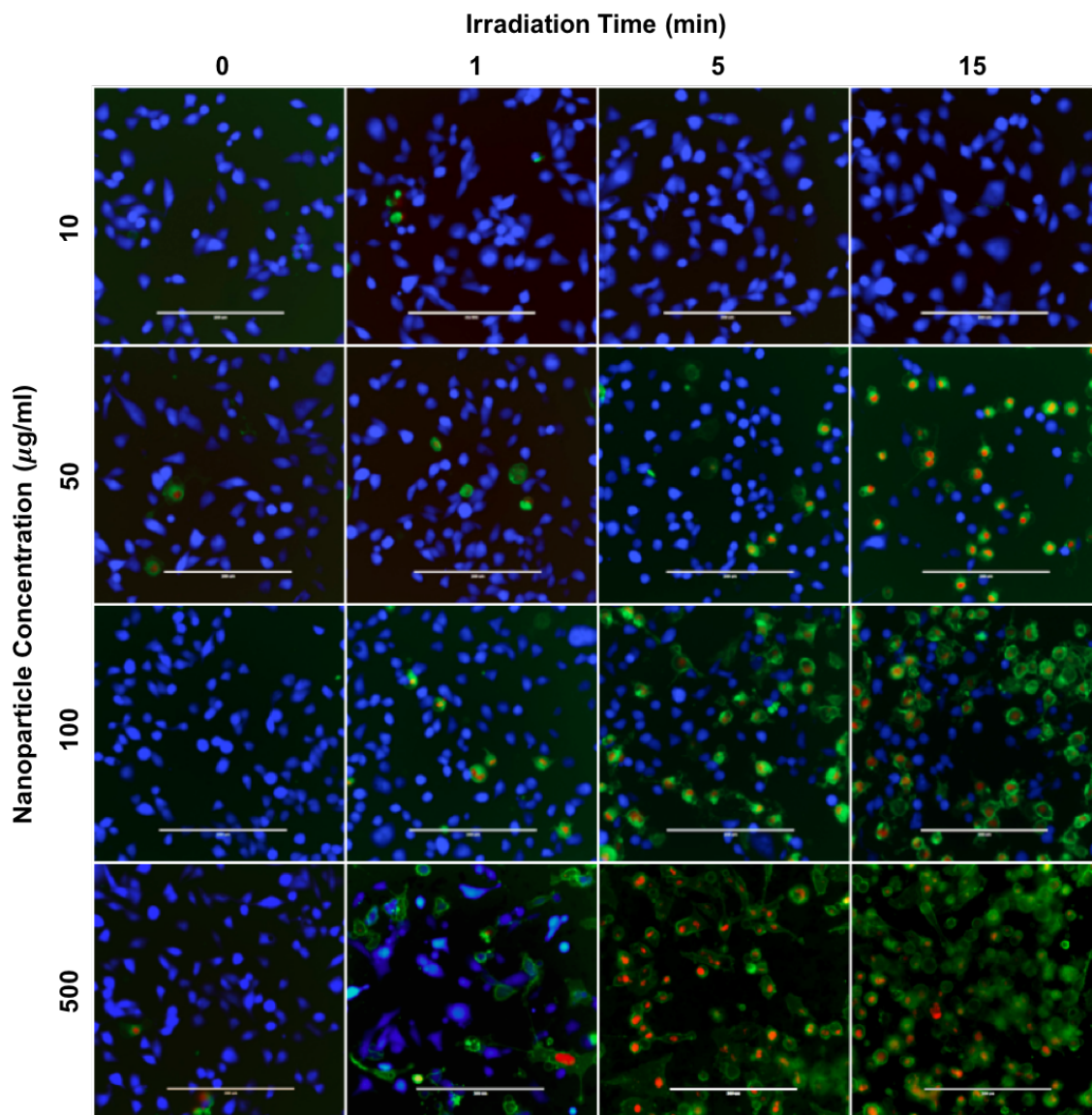


Figure 10. Fluorescence Microscopy of Cells Exposed to NPs for 1.5 Hours and Irradiation with an 808-nm Laser. Cells were exposed to 10, 50, 100, and 500 µg/mL NP concentrations for 0, 1, 5, and 15 minute irradiation time periods. Scale bar = 200 µm.

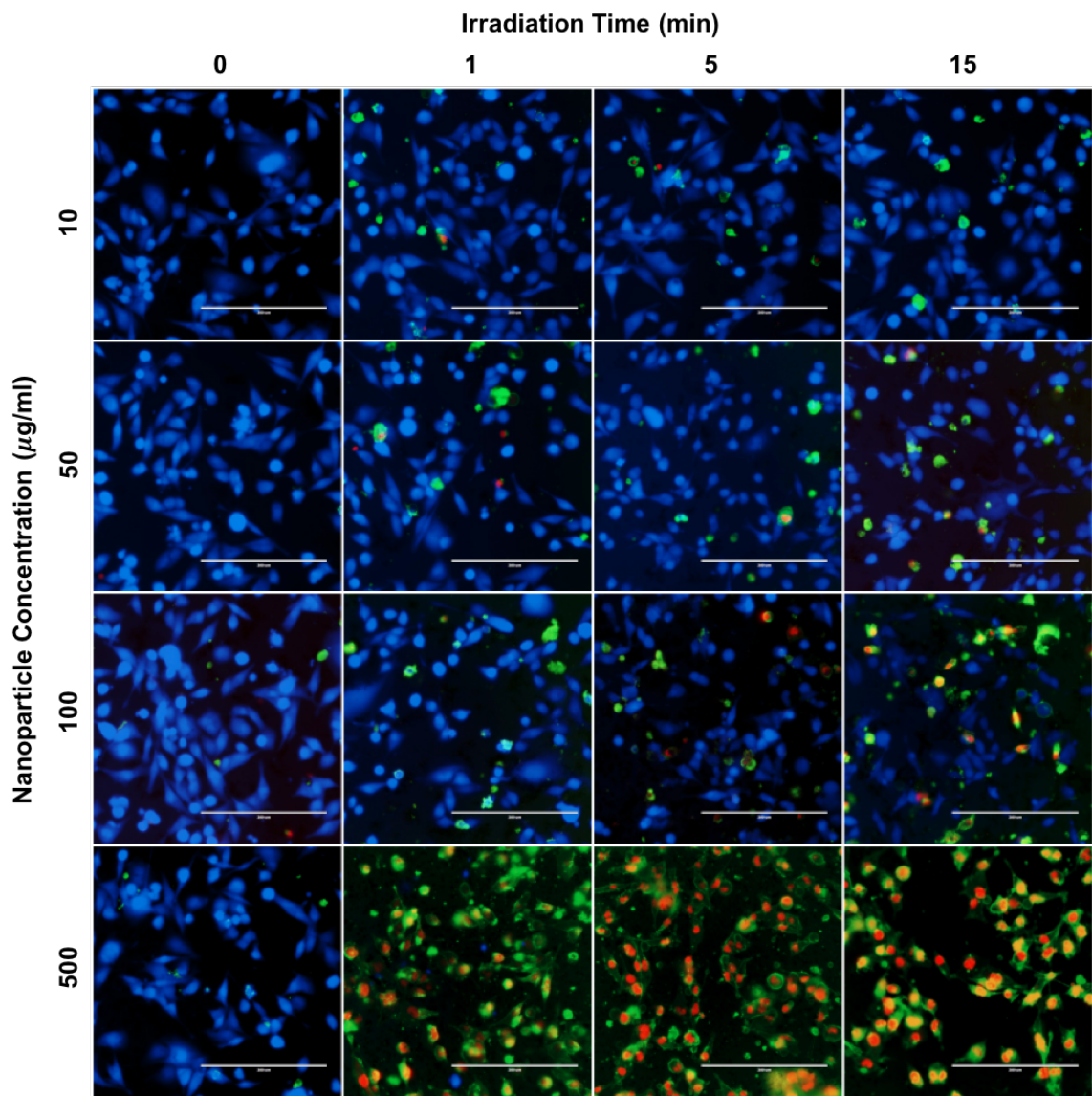


Figure 11. Fluorescence Microscopy of Cells Exposed to NPs for 6 Hours and Irradiation with an 808-nm Laser. Cells were exposed to 10, 50, 100, and 500 µg/mL NP concentrations for 0, 1, 5, and 15 minute irradiation time periods. Scale bar = 200 µm.

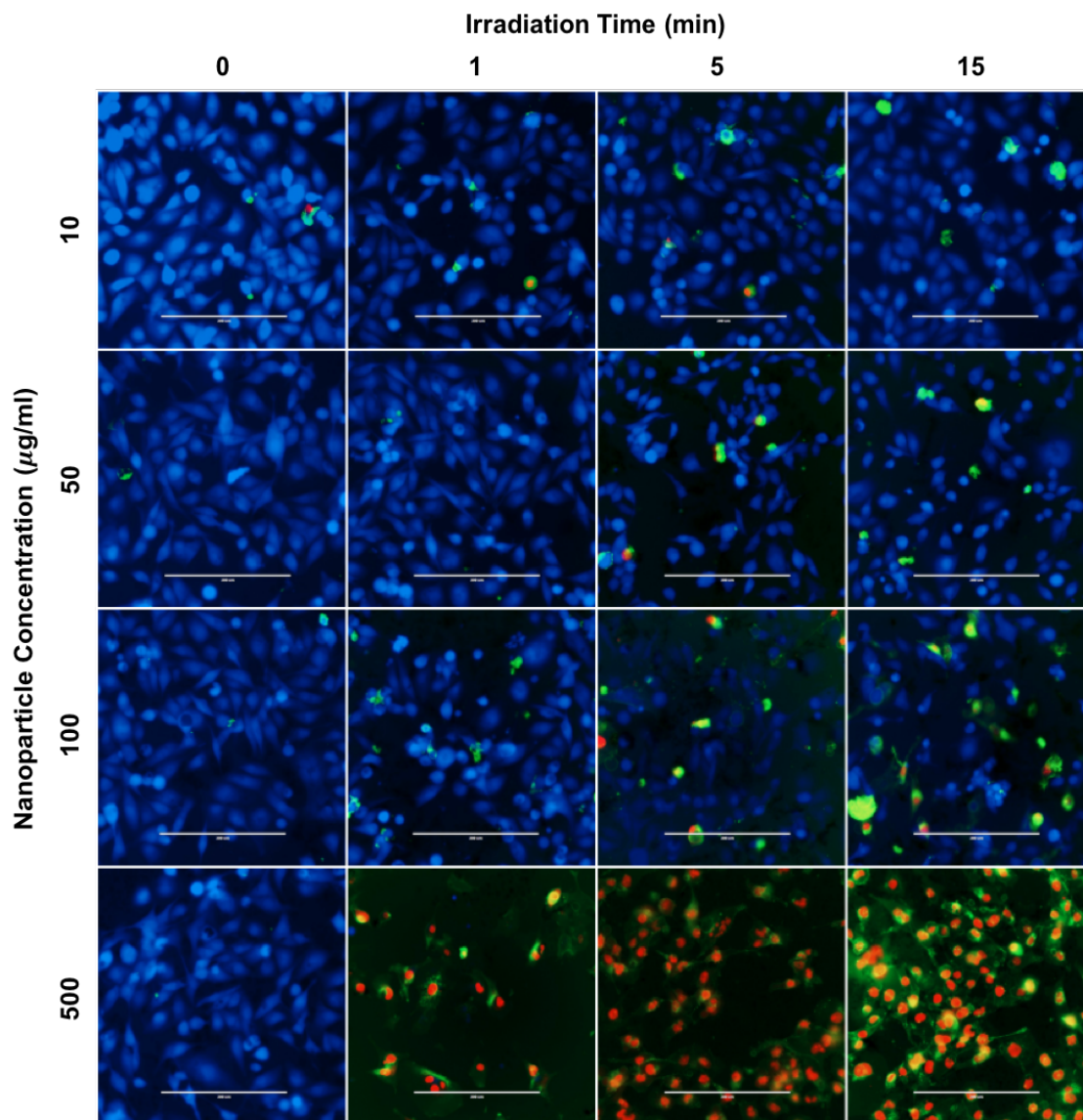


Figure 12. Fluorescence Microscopy of Cells Exposed to NPs for 12 Hours and Irradiation with an 808-nm Laser. Cells were exposed to 10, 50, 100, and 500 $\mu\text{g/mL}$ NP concentrations for 0, 1, 5, and 15 minute irradiation time periods. Scale bar = 200 μm .

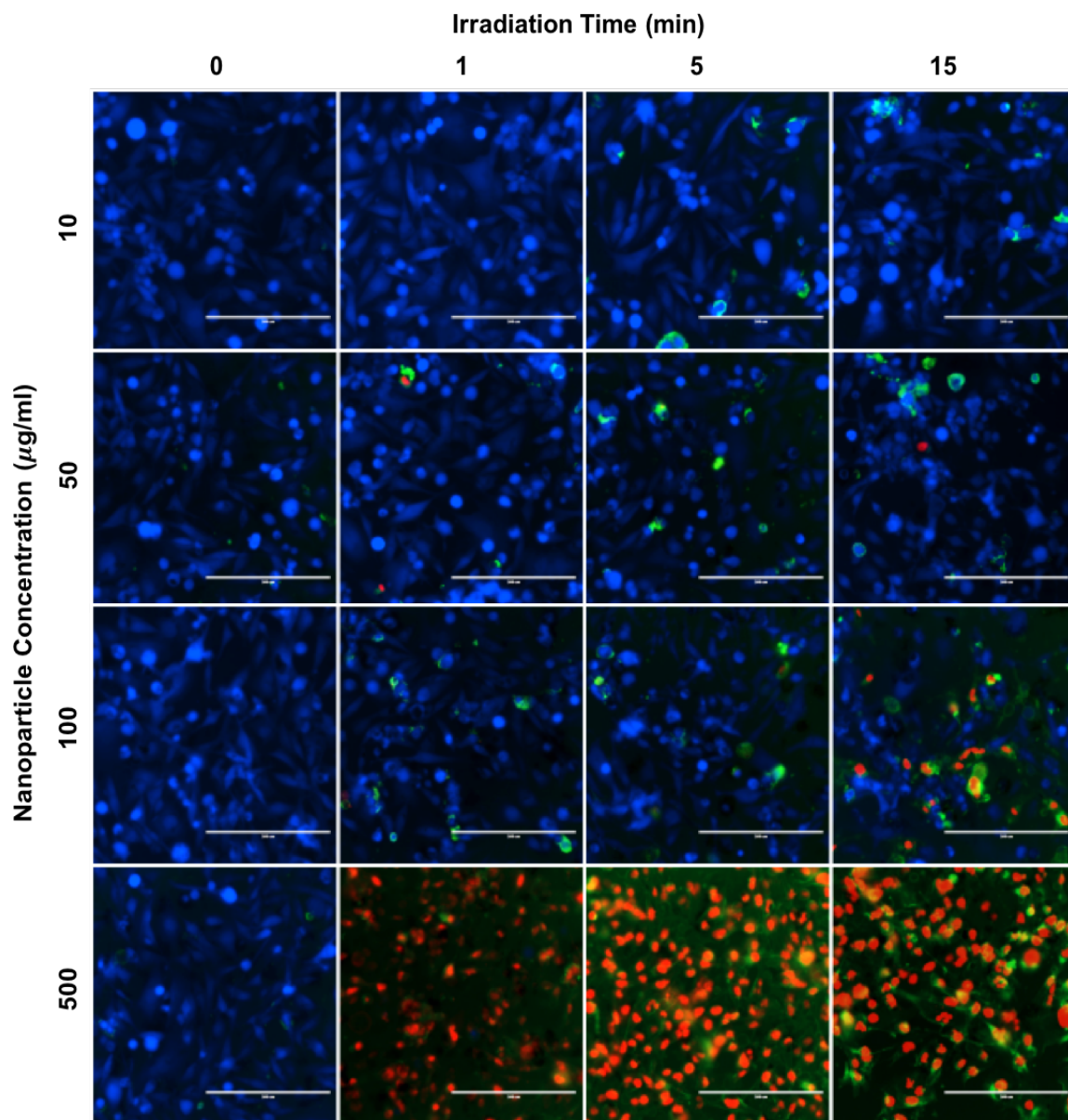


Figure 13. Fluorescence Microscopy of Cells Exposed to NPs for 24 Hours and Irradiation with an 808-nm Laser. Cells were exposed to 10, 50, 100, and 500 $\mu\text{g/ml}$ NP concentrations for 0, 1, 5, and 15 minute irradiation time periods. Scale bar = 200 μm .

3.5 Quantitative Analysis of Cell Death by Flow Cytometry

The cellular response to PEDOT NP-mediated photothermal therapy was quantitatively analyzed using flow cytometry to obtain log-log pseudocolor density plots with the apoptotic fluorescence intensity on the x-axis and the necrotic fluorescence intensity on the y-axis. The pseudocolor plots display the relative population density of the cell populations, denoting areas of high and low population density. Each dot displayed on the plots represents a single cell of the population, while the colors presented in the plots refer to the density of the cells relative to one another and is not an indicator of the spectra that the cells emit. Blue and green correspond to areas of lower cell density, red and orange are areas of high cell density, and yellow is mid-level. Gating of the negative and positive controls established three distinct regions within the plot: the live, apoptotic, and necrotic cells in parts A, B, and C, respectively, of Figure 14. Gating was determined by selecting the distinct population in the forward scatter vs. side scatter plots, and then re-analyzing that population as a function of the fluorophores. Gates were placed to closely surround the cell population and adequately separate it from the other control populations.

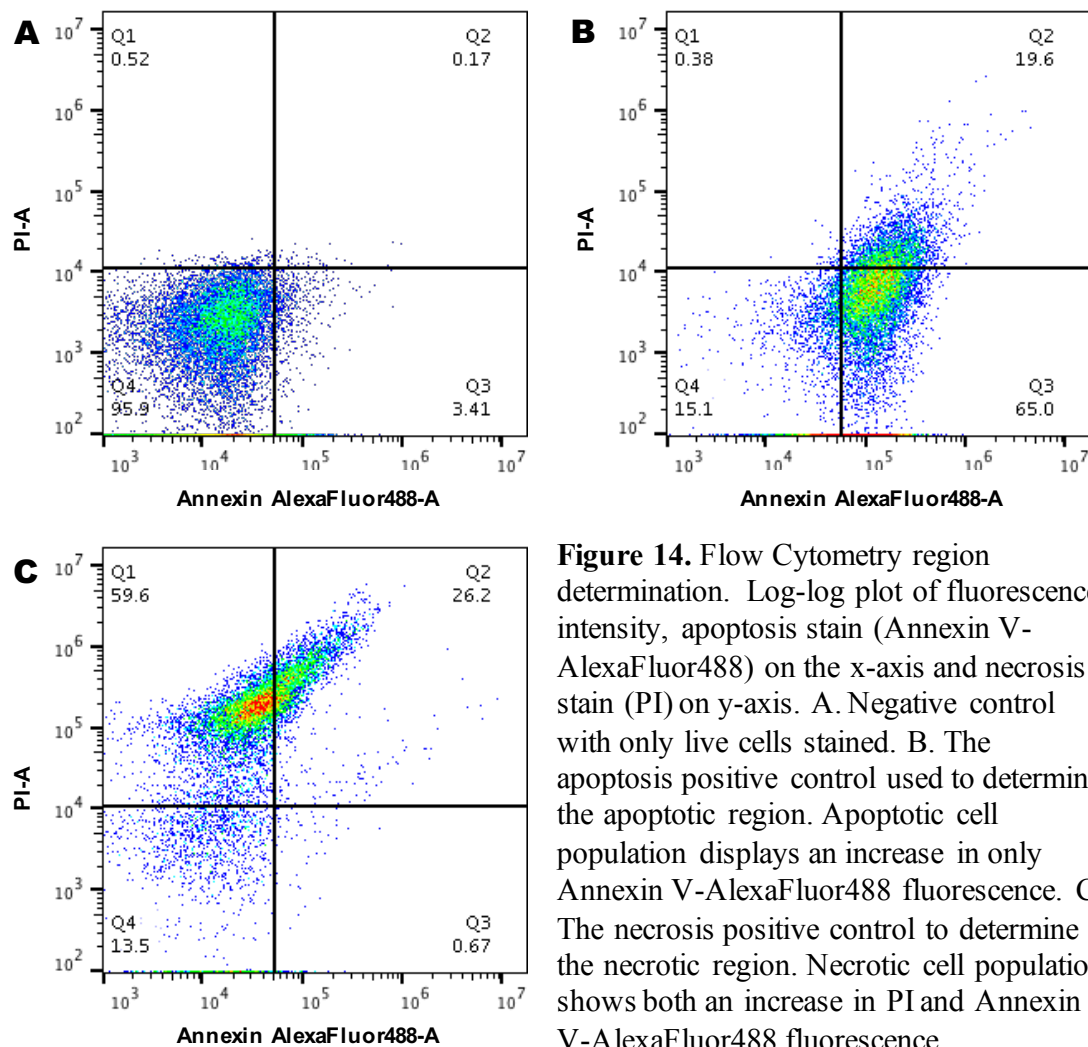


Figure 14. Flow Cytometry region determination. Log-log plot of fluorescence intensity, apoptosis stain (Annexin V-AlexaFluor488) on the x-axis and necrosis stain (PI) on y-axis. A. Negative control with only live cells stained. B. The apoptosis positive control used to determine the apoptotic region. Apoptotic cell population displays an increase in only Annexin V-AlexaFluor488 fluorescence. C. The necrosis positive control to determine the necrotic region. Necrotic cell population shows both an increase in PI and Annexin V-AlexaFluor488 fluorescence.

After region determination, samples were analyzed after PEDOT NP-mediated photothermal therapy. Figure 15 presents the log-log plots collected from cell samples that were exposed to 500 $\mu\text{g/ml}$ NP suspensions and irradiated for 15 minutes with the NIR laser after all incubation time periods. After 1.5 hours of co-incubation with 500 $\mu\text{g/ml}$ NPs, $\sim 75\%$ of the cell population was apoptotic and $\sim 13\%$ was necrotic after 15 minutes of irradiation. The fluorescence microscopy images complemented these results by the primarily green fluorescence observed at this time point. At the same NP concentration and irradiation time, the percentage of apoptotic cells decreased as the

incubation time increased; concurrently, an increase in necrotic cell death was seen. At the 6-hour time point, ~66% of the cells had undergone an apoptotic cell death and ~15% had undergone necrosis, while at the 12-hour time point ~50% of the cells were apoptotic and ~35% were necrotic. After 24 hours of incubation, necrotic cell death became the dominant cell death pathway with greater than 50% of the cell population undergoing necrosis and ~35% undergoing apoptosis. The fluorescence images at this time point also predominantly displayed red fluorescence from the PI, supporting the quantitative data from the flow cytometry. Figure 16 displays the percentage of live, apoptotic, and necrotic cells within a cell population for every parameter quantitatively tested.

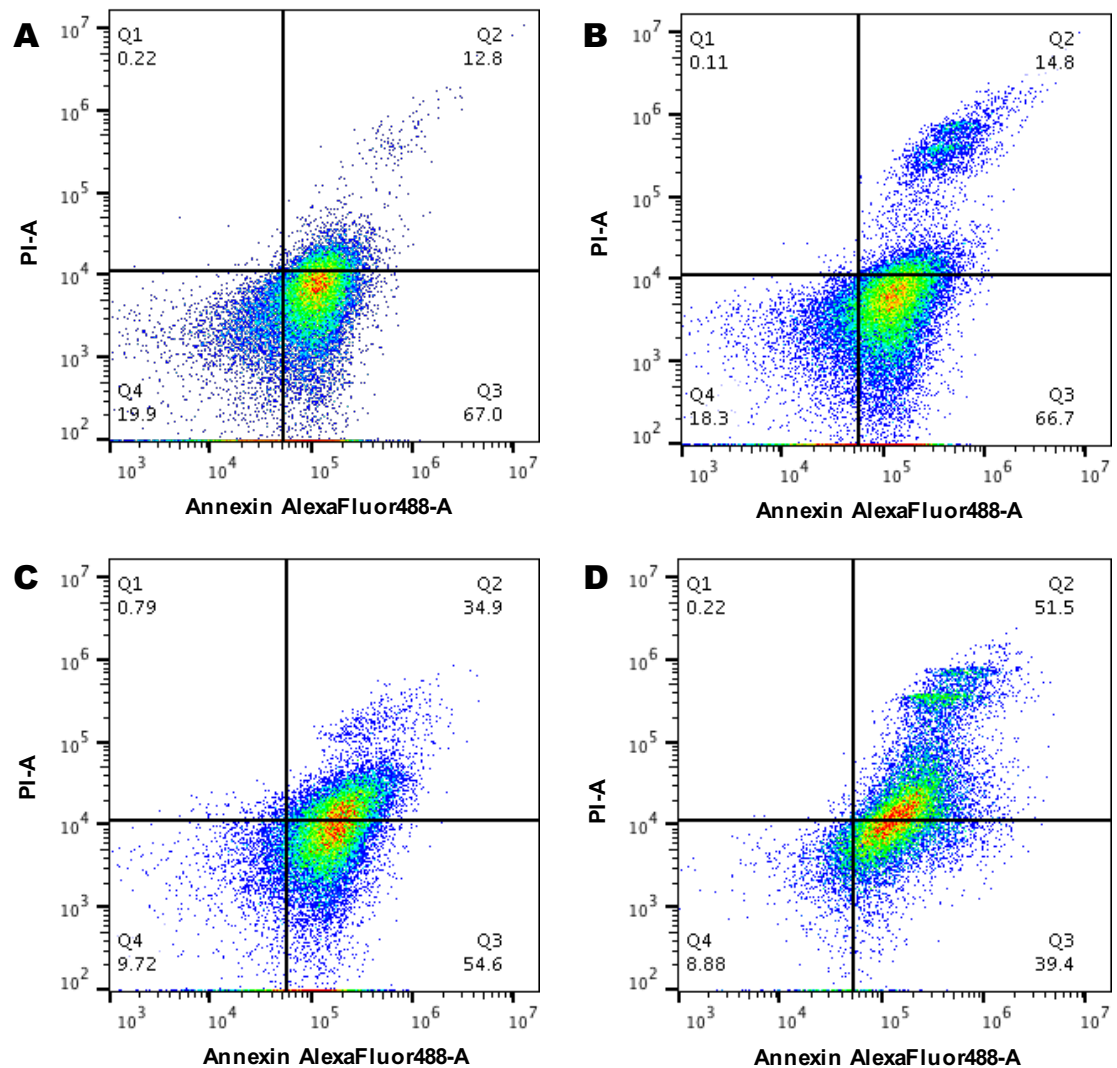
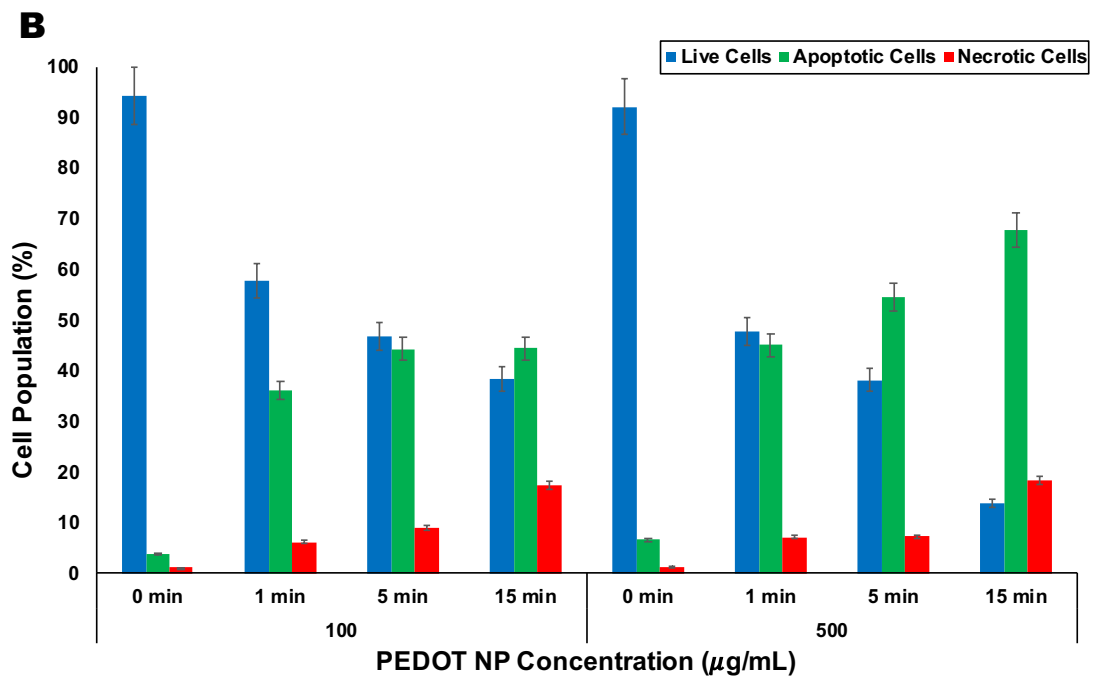
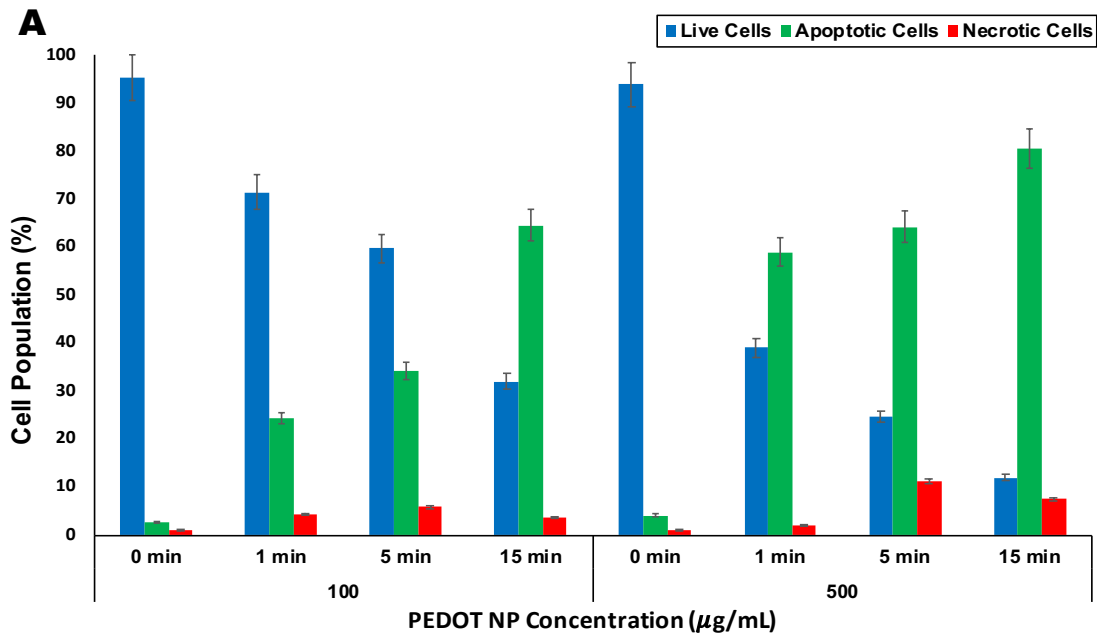


Figure 15. Quantitative Analysis of Cell Death Pathways by Flow Cytometry. Log-log plot of fluorescence intensity, apoptosis stain (Annexin V-AlexaFluor488) on the x-axis and necrosis stain (PI) on y-axis. All samples were treated with 500 $\mu\text{g/ml}$ of nanoparticles and irradiated for 15 minutes using a NIR laser. Cells co-incubated with nanoparticles for A. 1.5 hours, B. 6 hours, C. 12 hours, D. and 24 hours.



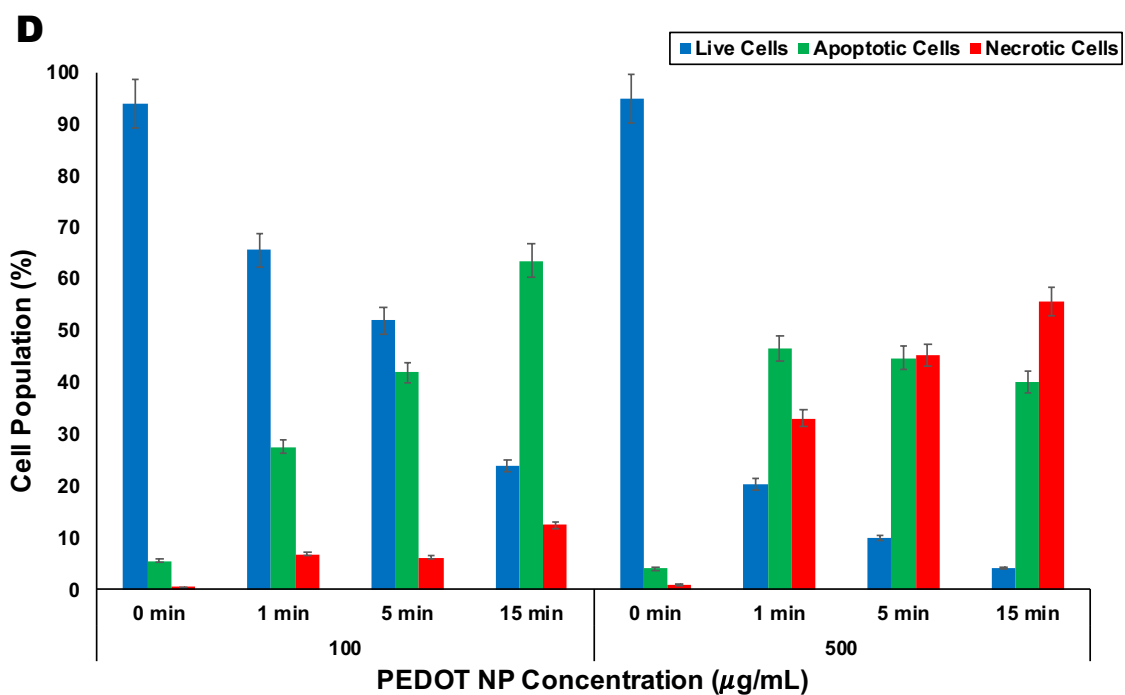
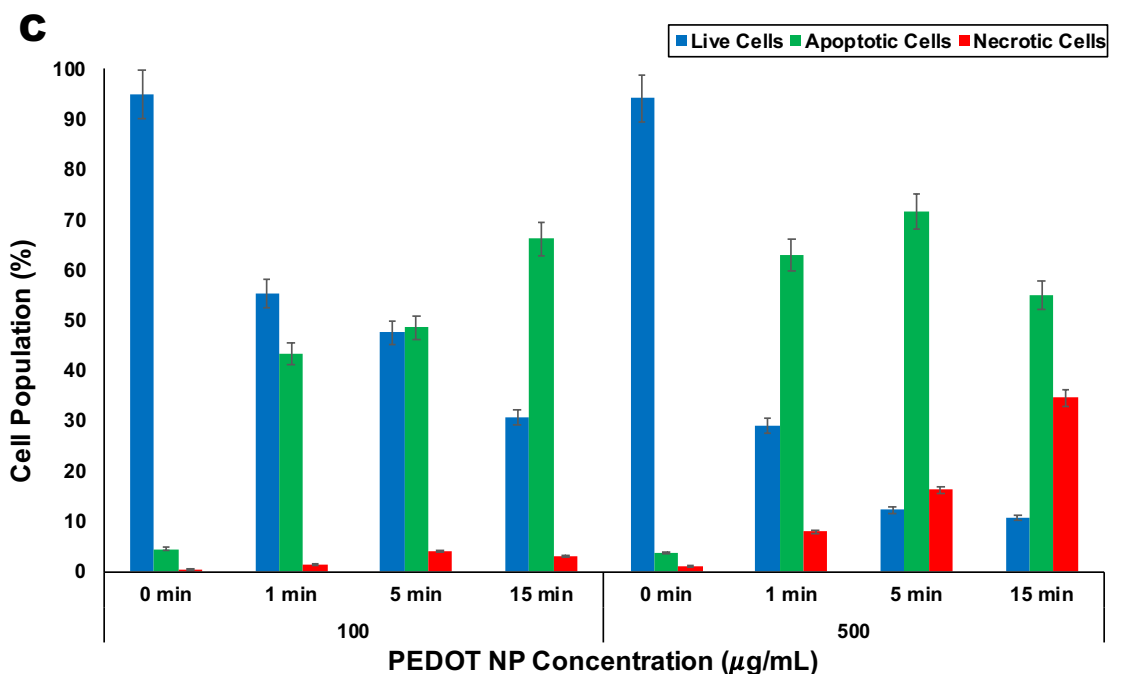


Figure 16. Flow Cytometry Data After NP Incubation Period and Irradiation with an 808-nm Laser. Blue indicates the percentage of live cells within the population, green indicates the percentage of apoptotic cells, and red indicates the percentage of necrotic cells. Apoptotic and necrotic cells were determined by their overall level of fluorescence by either Annexin V AlexaFluor488 or PI. Live cells were determined by their lack of fluorescence from these two biochemical markers. (A) 1.5, (B) 6, (C) 12, (D) and 24-hour incubation time periods.

3.6 Caspase Expression in Cell Death

Caspase-3/7 expression was analyzed in the breast cancer cells after NP-mediated PTT in order to confirm cell apoptosis (Figures 17 and 18). No fluorescence was observed at the 10-50 $\mu\text{g/ml}$ concentrations for all incubation times, which closely matches the previous data on the cell viability seen at these concentrations. The 1.5-hour NP-cell exposure time displayed a visually higher level of fluorescence for both the 100 and 500 $\mu\text{g/ml}$ concentrations as compared to the 24-hour NP-cell exposure time (compare bottom two rows in Figure 17 to bottom two rows in Figure 18). The quantified data from the fluorescence images presents a 6-fold decrease in fluorescence intensity density from the 1.5-hour time point to the 24-hour time point at all irradiation time periods after exposure to 500 $\mu\text{g/ml}$ NPs (Figure 19). Since caspase-3/7 is an indication of apoptotic cell death activation, the data verifies that the peak of apoptotic cell death occurs after exposure to 500 $\mu\text{g/ml}$ NPs and 1.5 hours of NP-cell incubation.

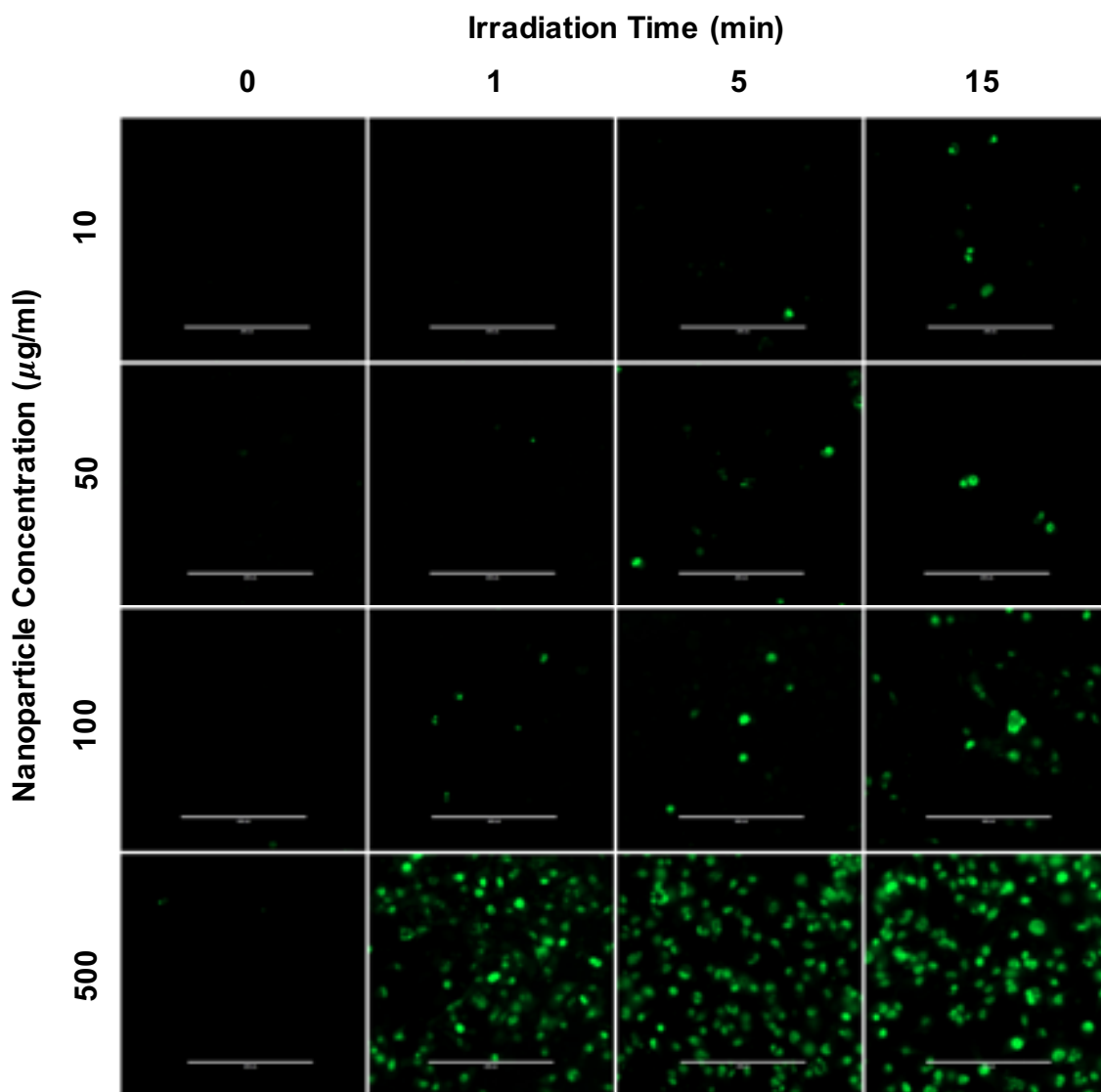


Figure 17. Fluorescence Microscopy Images of Caspase-3/7 Expression in Cell Populations After 1.5 Hours of Co-Incubation with NPs and Irradiation with an 808-nm Laser. Caspase expression was analyzed by using CellEvent™ Caspase-3/7 Green Detection Reagent in order to confirm apoptotic cell death.

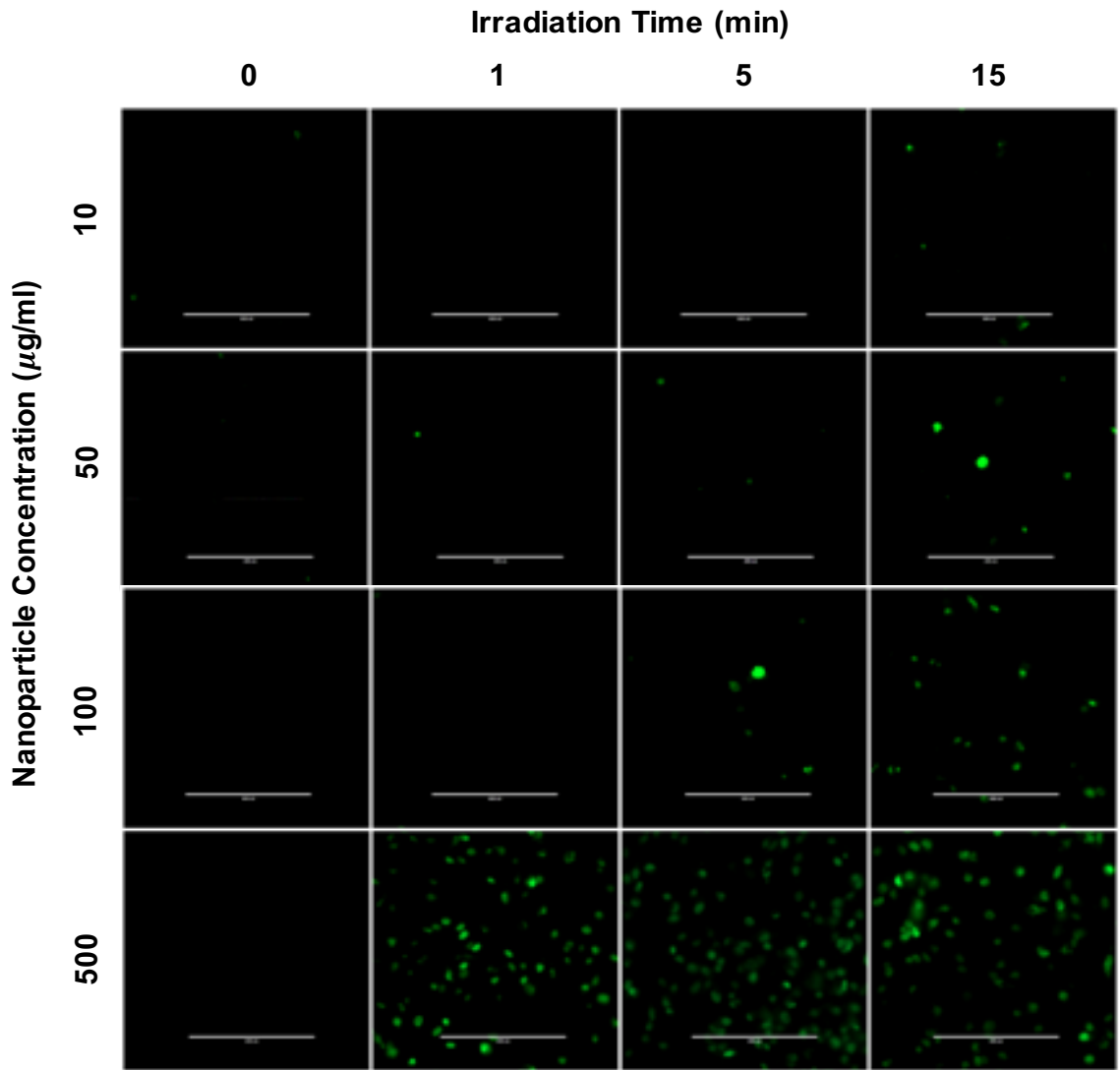


Figure 18. Fluorescence Microscopy Images of Caspase-3/7 Expression in Cell Populations After 24 Hours of Co-Incubation with NPs and Irradiation with an 808-nm Laser. Caspase expression was analyzed by using CellEvent™ Caspase-3/7 Green Detection Reagent in order to confirm apoptotic cell death.

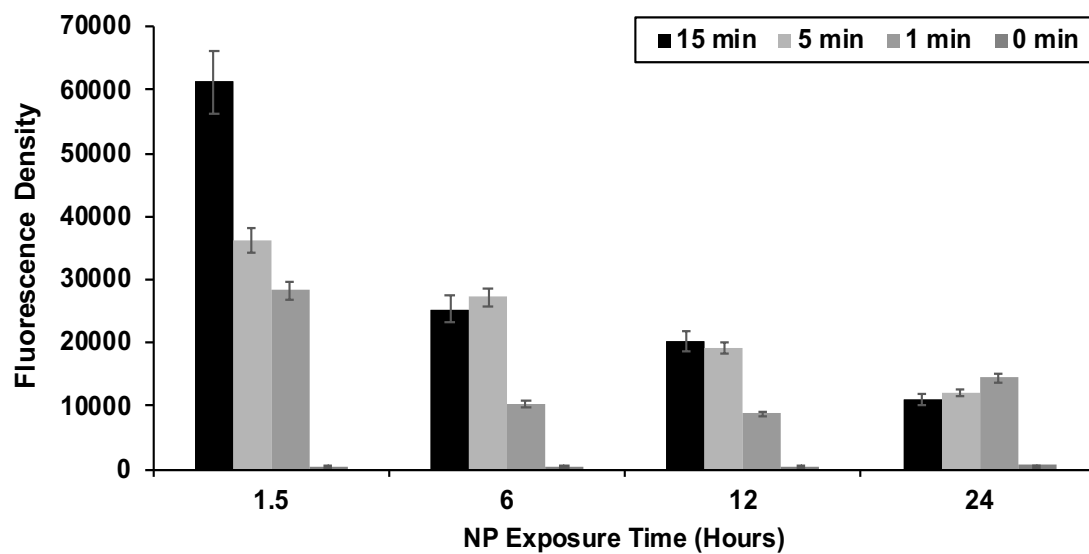


Figure 19. Fluorescence Density Indicative of Caspase-3/7 Expression. Standard deviations were calculated from 3 separate images of each variable as a function of the NP exposure time (hours). Fluorescence intensity quantification of microscopy images was performed using ImageJ software.

Chapter IV

DISCUSSION AND CONCLUSION

4.1 Discussion

In this study, we reported the preparation of PEDOT NPs by oxidative-emulsion polymerization, which yielded spherical NPs less than 100 nm. The use of DBSA and PSS-co-MA as anionic surfactants in conjunction with the positively charged polymer contributed to the relatively negative zeta potential of the NPs. In fact, the negative zeta potential displayed by these NPs aided in their overall high colloidal stability by interparticle charge repulsion.¹⁵ The surfactants also acted as dopants, which stabilized the NPs in the oxidized state by becoming part of the polymer backbone.¹⁶ The polymer being in the oxidized state is absolutely critical for their absorbance in the NIR region; in the reduced state, the polymer's absorbance blueshifts to the visible range (data gathered by previous students in the Betancourt lab).

The decision to use Nile Red as a fluorescent indicator to study the cellular internalization of the PEDOT NPs came from the fact that it is a hydrophobic dye that is readily miscible in many organic solvents. Nile Red's solubility in toluene allowed for it to be easily incorporated into the organic phase of the NP preparation. Upon addition of the organic phase to the aqueous phase, the Nile Red dye would shy away from the surrounding aqueous environment and settle within the hydrophobic core of the NPs. Additionally, an ideal characteristic of the dye is that it is almost nonfluorescent in polar solvents but undergoes fluorescence enhancement and large absorption and emission blue shifts in non-polar environments.⁶⁵ This characteristic was the determining factor over the

use of other fluorescent dyes, such as rhodamine and FITC, since there would be no question on whether the fluorescence was coming from the encapsulated dye inside of the NPs or from the released dye outside of the NPs.

The physical encapsulation of Nile Red by the PEDOT NPs is a strong indicator for the potential encapsulation of other organic compounds, such as chemotherapeutic agents. Hydrophobic drugs could be encapsulated in these conductive polymer nanoparticle photothermal agents by introducing the drug into the organic phase before creation of the emulsion. Furthermore, the cellular internalization data indicate that the NPs surround the nucleus once internalized by the cell, making them ideal candidates for the delivery of drugs that carry out their intended purpose in the nuclei of cells. The utilization of PEDOT NPs as both a drug delivery agent and a photothermal agent for combination therapy could potentially increase the efficacy of the nanoagent for the eradication of tumors.

MDA-MB-231 breast cancer cells were used as the *in vitro* model of cancer for all experimental cell studies. This cell line is a triple negative cell line that lacks expression of the estrogen, progesterone, and human epidermal growth factor 2 (HER2) receptors. Triple negative breast cancer tends to be the deadliest and most aggressive form of breast cancer, limiting therapeutic options to surgery and chemotherapy. Therefore, the work accomplished in this thesis demonstrating the effectiveness of PEDOT NPs with this cell line is significant.

A major goal of this study was to qualitatively and quantitatively analyze the role of the cell death response during nanoparticle-mediated PTT in order to better understand

and optimize this localized treatment of cancer. Our hypothesis that the interaction of PEDOT NPs within breast cancer cells would activate distinct cell death pathways as a result of photothermal ablation was shown to be accurate based on the experimental variables tested. NP-cell incubation time proved to be a vital factor in the activation of different cell death pathways, with the lower incubation times showing prominent apoptotic cell death, while the higher incubation times displayed more necrotic cell death. This difference in cell death activation could be due to an increase in NP uptake and internalization by the cells as well as by the differences in intracellular nanoparticle distribution at the higher incubation times, as displayed by the NP internalization confocal images. After the 24-hour incubation, there was an observable increase in the overall uptake of NPs, as well as an increase in NP accumulation around the nucleus. The aggregation of NPs surrounding the perinuclear region could contribute to necrosis becoming the dominant pathway at this time point. Conversely, the 1.5-hour time point saw an increase in the apoptotic pathway when the NPs were predominantly surrounding the plasma membrane. Variation in NP concentration and irradiation time for cells that had similar NP exposure time seemed to have little effect on the stimulation of different cell deaths. However, the live cell population did decrease consistently as NP concentration and irradiation time increased, despite NP-cell incubation time.

This work has demonstrated our ability to control the mechanisms of cell death by changing the parameters of PEDOT NP exposure and NIR radiation time. Being able to tune the mode of cell death between apoptosis and necrosis provides the opportunity to gear this cancer therapeutic towards the field of immunotherapy. Up until very recently, apoptosis was believed to not provoke any kind of inflammatory immune response.⁴⁴

However, many publications have supported the conclusion that apoptotic cells can also produce and secrete immunostimulatory proteins, or damage-associated molecular patterns (DAMPs).⁶⁶⁻⁶⁸ DAMPs, such as heat shock proteins, calreticulin, high mobility group B1, and extracellularly secreted ATP, generate an antigen-specific immune response that acts on both the innate and adaptive immune systems.⁶⁶ This novel form of cell death is termed “immunogenic cell death” (ICD), and is usually used in the context of anti-tumor therapeutics for their vaccine-like implications.⁴⁴ ICD inducers may include chemotherapeutic drugs and irradiation.⁶⁸ Therefore, the ability to elicit an apoptotic cell death using nanoparticle-mediated PTT displays its potential for immunotherapy by possibly being able to evoke an ICD.

Pattani et al. reported similar cellular internalization results using gold nanorods (GNRs).⁵⁸ After 1.5 hours of GNR incubation with colon cancer cells, the GNRs were membrane bound and starting to be internalized by lysosomes. At the 24-hour time point, the GNRs were localized to the perinuclear space and hypothesized to be in closer proximity to organelles. The internalization of these GNRs closely matches the PEDOT NP internalization process reported in this thesis. However, the GNR zeta potential was observed to be 50.6 mV due to a cationic surfactant present on the surface. Pattani et al. claimed the positive nature of the GNRs aided in the internalization process at the negatively charged plasma membrane, but the PEDOT NPs presented in this work had an observed zeta potential of -30.9 mV, which directly contradicts this claim. Furthermore, the authors observed their highest apoptotic percentage (~18.5%) after the 24-hour incubation period, when the GNRs had localized in the perinuclear space.⁵⁸ This data is also conflicting with the reported ~75% apoptotic cell death seen in this study after only

1.5 hours of incubation.

Future work that would aid in achieving our long-term goal involves investigation of dual chemotherapy/photothermal therapy using drug-loaded PEDOT NPs.

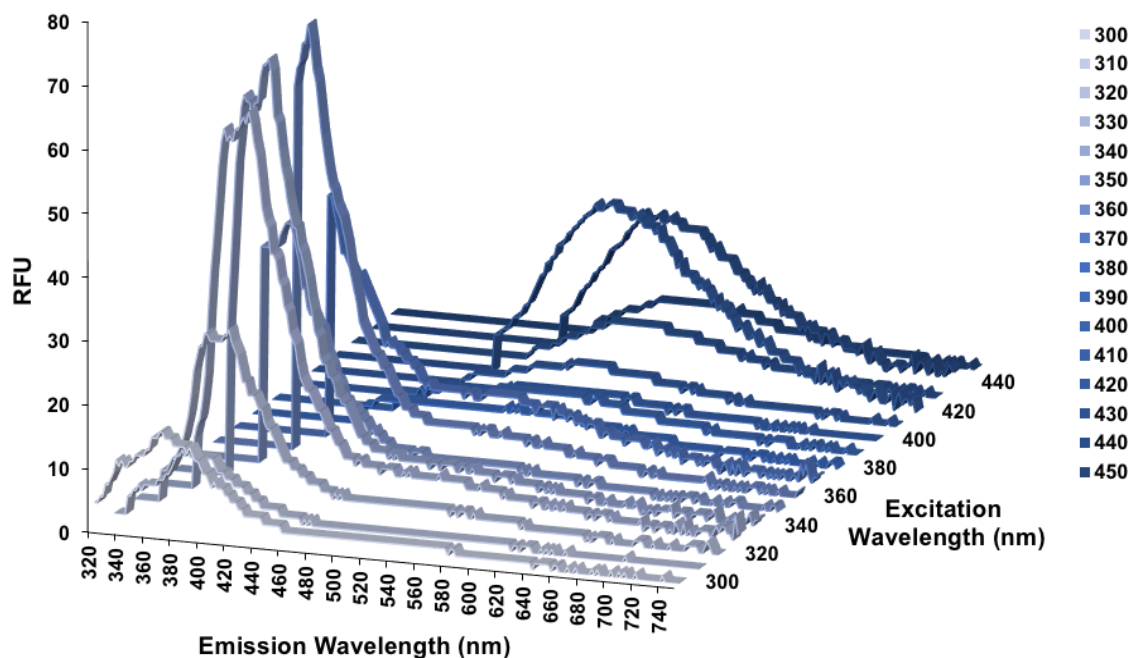
Encapsulation of a chemotherapeutic agent, such as doxorubicin, within PEDOT NPs can be thoroughly investigated by analyzing drug encapsulation efficiency, cytotoxicity, adequate NIR absorption, drug release with and without NIR irradiation, and cell death mechanisms caused by PTT using these doxorubicin NPs. Additionally, analysis of immunostimulatory proteins expressed by cells undergoing immunogenic cell death could be explored.

4.2 Conclusions

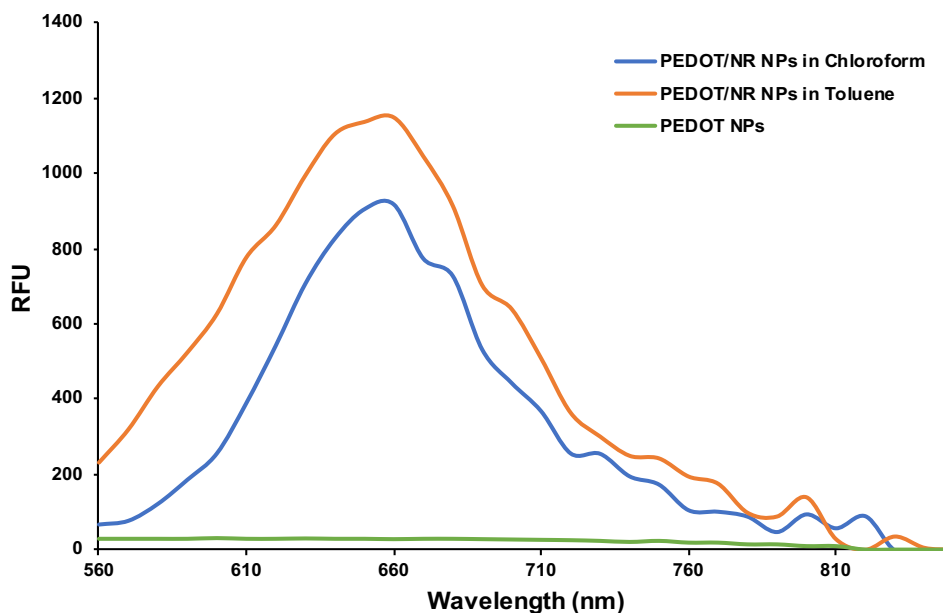
PEDOT NPs were confirmed to be cytocompatible, yet effective photothermal agents at the ablation of cancer. The NPs successfully absorbed light in the NIR region and exhibited the optimal size of <100 nm as confirmed by dynamic light scattering and SEM. PEDOT NPs displayed photothermal properties, being able to generate a maximum change in temperature of approximately 30°C at a 500 $\mu\text{g/ml}$ concentration. This increase in temperature was sufficient to cause total cell death after 5-15 minutes of irradiation at this NP concentration. Despite having an overall negative zeta potential, the NPs were internalized within the cells through what appeared to be endosomes, even at the lowest incubation time of 1.5 hours. The location of the NPs within the cell also proved to be time dependent, with the majority of the NPs at the plasma membrane after 1.5 hours and then at the perinuclear region after 24 hours of incubation. The qualitative and quantitative data carried out by fluorescence microscopy and flow cytometry revealed

that 60-75% of MDA-MB-321 breast cancer cells died by primarily apoptosis after being exposed to 100-500 $\mu\text{g/ml}$ PEDOT NPs for 1.5 hours and irradiated with a NIR laser for 15 minutes. The 10-50 $\mu\text{g/ml}$ concentration had little-to-no effect on cell viability for any of the NP incubation time periods, indicating that this range of PEDOT NP concentrations was too low to elicit any prominent kind of cell death. Apoptosis was also the preferred cell death pathway after being exposed to 100-500 $\mu\text{g/ml}$ concentration for 6 and 12-hour time periods. After 24 hours of exposure to the 100 and 500 $\mu\text{g/ml}$ NPs, the primary cell death pathway observed was necrosis, with >50% of the cell population undergoing a necrotic cell death. As the NP exposure time with the cells increased, the amount of necrotic cell death seen also increased for the 100 and 500 $\mu\text{g/ml}$ concentrations. Analysis of the role of caspase-3/7 expression in cell death confirmed these finding by displaying a higher degree of fluorescence in the 1.5-hour time point. The fluorescence intensity continuously decreased as the incubation time increased, indicating that caspase expression is also decreasing. Considering caspase-3/7 is a hallmark of apoptotic cell death activation, the maximum caspase expression observed at the 1.5-hour incubation time verifies the maximum apoptosis at this time point. The studies reported in this work clearly identify the cell death pathways as a function of the experimental parameters we set out to address for NP-mediated photothermal therapy. Therefore, understanding the mechanisms of cell death caused by NP-mediated photothermal therapy is crucial to predict and optimize the efficacy of this novel treatment against malignant tumor cells that are unresponsive to conventional cancer therapies.

APPENDIX



Appendix Figure A1. PEDOT NP fluorescence spectrum after excitation at multiple wavelengths. NPs were excited in 10 nm increments ranging from 300-450 nm, with a peak fluorescence seen at 390 nm after exciting at 360 nm.



Appendix Figure A2. Fluorescence spectrum of PEDOT NPs, PEDOT/NR NPs made with chloroform, and PEDOT/NR NPs made with toluene. Samples were excited at 530 nm.

REFERENCES

- 1) Siegel, R.L., Miller, K.D., Jemal, A. (2017) Cancer Statistics. *CA Cancer J Clin.* **67**, 7-30.
- 2) Miller, K.D., Siegel, R.L., Lin, C.C., Mariotto, A.B., Kramer, J.L., Rowland, J.H., Stein, K.D., Alteri, R., Jemal, A. (2016) Cancer treatment and survivorship statistics. *CA Cancer J Clin.* **66**, 271-289.
- 3) Chen, Q., Xu, L., Liang, C., Wang, C., Peng, R., Liu, Z. (2016) Photothermal therapy with immune adjuvant nanoparticles together with checkpoint blockade for effective cancer immunotherapy. *Nature Comm.* **7**, 1-13.
- 4) Fay, B.L., Melamed, J.R., Day, E.S. (2015) Nanoshell-mediated photothermal therapy can enhance chemotherapy in inflammatory breast cancer cells. *Int J Nanomedicine.* **10**, 6931-6941.
- 5) Arranja, A.G., Pathak, V., Lammers, T., Shi, Y. (2017) Tumor-targeted nanomedicines for cancer theranostics. *Pharm Res.* **115**, 87-95.
- 6) Trock, B.J., Leonessa, F., Clarke, R. (1997) Multidrug resistance in breast cancer: a meta-analysis of MDR1/gp170 expression and its possible functional significance. *J Natl Cancer Inst.* **89**, 917-993.
- 7) Curigliano, G., Cardinale, D., Suter, T., Plataniotis, G., de Azamuja, E., Sandri, M.T., Criscitiello, C., Goldhirsch, A., Cipolla, C., Roila, F. (2012) Cardiovascular toxicity induced by chemotherapy, targeted agents and radiotherapy: ESMO Clinical Practice Guidelines. *Ann Oncol.* **23**, 155-166.

- 8) Early Breast Cancer Trialists' Collaborative Group (EBCTCG), Davies, C., Godwin, J. (2011) Relevance of breast cancer hormone receptors and other factors to the efficacy of adjuvant tamoxifen: patient-level meta-analysis of randomized trials. *Lancet*. **378**, 771-784.
- 9) Chen, H., Zhang, W., Zhu, G., Xie, J., Chen, X. (2017) Rethinking cancer nanotheranostics. *Nat. Rev. Mater.* 17024: doi:10.1038/natrevmats.2017.24.
- 10) Fan, Z., Fu, P., Yu, H., Ray, P. (2014) Theranostic nanomedicine for cancer detection and treatment. *J. Food and Drug Anal.* **22**, 3-17.
- 11) Xie, J., Lee, S., Chen, X. (2010) Nanoparticle-based theranostic agents. *Adv Drug Deliv Rev.* **62**, 1064-1079.
- 12) Bray, F., Moller, B. (2006) Predicting the future burden of cancer. *Nat Rev Cancer.* **6**, 63-74
- 13) Famulok, M., Hartig, J., Mayer, G. (2007) Functional aptamers and aptazymes in biotechnology, diagnostics, and therapy. *Chem Rev.* **107**, 3715-3743.
- 14) De Jong W.H. and Borm P.J. (2008) Drug delivery and nanoparticles: Applications and hazards. *Int J Nanomedicine.* **3**, 133-149.
- 15) Cantu T, Rodier B, Iszard Z, Kilian A, Pattani V, Walsh K, Weber K, Tunnell J, Betancourt T, Irvin J. (2016) Electroactive Polymer Nanoparticles Exhibiting Photothermal Properties. *J Vis Exp* **107**, e5363.
- 16) Cantu, T., Walsh, K., Pattani, V.P., Moy, A.J., Tunnell, J.W., Irvin, J.A., Betancourt, T. (2017) Conductive polymer-based nanoparticles for laser-mediated photothermal ablation of cancer: synthesis, characterization, and in vitro evaluation. *Int J Nanomedicine.* **12**, 615-632.

- 17) Kaur, P., Aliru, M.L., Chadha, A.S., Asea, A., Krishnan, S. (2016) Hyperthermia Using Nanoparticles – Promises and Pitfalls. *Int J Hyperthermia*. **32**, 76-88.
- 18) Fernandez Cabada, T., de Pablo, C. S., Serrano, A. M.; Guerrero Fdel, P., Olmedo, J. J., Gomez, M. R. (2012) Induction of Cell Death in a Glioblastoma Line by Hyperthermic Therapy based on Gold Nanorods. *Int J Nanomedicine*. **7**, 1511–1523.
- 19) Tang, Y., McGoron, A.J. (2009) Combined effects of laser-ICG photothermotherapy and doxorubicin chemotherapy on ovarian cancer cells. *J Photochem and Photobio Bio*. **97**, 138-144.
- 20) Cheng, L., Wang, C., Feng, L. Z., Yang, K. & Liu, Z. (2014) Functional nanomaterials for phototherapies of cancer. *Chem. Rev.* **114**, 10869-10939.
- 21) Huang, X., Jain, P.K., El-Sayed, I.H., El-Sayed, M.A. (2007) Plasmonic photothermal therapy (PPTT) using gold nanoparticles. *Lasers Med Sci*. **23**, 217-228.
- 22) Hessel, C.M., Pattani, V., Rasch, M., Panthani, M.G., Koo, B., Tunnell, J.W., Korgel, B.A. (2011) Copper Selenide Nanocrystals for Photothermal Therapy. *Nano Lett*. **11**, 2560-2566.
- 23) Kobayashi, H.; Watanabe, R.; Choyke, P.L. (2013) Improving conventional enhanced permeability and retention (EPR) effects; what is the appropriate target? *Theranostics*. **4**, 81–89.
- 24) Bardhan, R., Lal, S., Joshi, A., Halas, N. J. (2011) Theranostic Nanoshells: From Probe Design to Imaging and Treatment of Cancer. *Acc. Chem. Res.* **44**, 936.

- 25) Danhier F, Feron O, Pr at V (2010) To exploit the tumor microenvironment: passive and active tumor targeting of nanocarriers for anti-cancer drug delivery. *J Control Release*. **148**, 135-146.
- 26) Byrne JD, Betancourt T, Brannon-Peppas L (2008) Active targeting schemes for nanoparticle systems in cancer therapeutics. *Adv Drug Deliv Rev*. **60**, 1615-1626.
- 27) Lovell, F., Jin, C., Huynh, E., Jin, H., Kim, C., Rubinstein. J., Chan, W., Cao, W., Wang, L., Zheng, G. (2011) Porphysome nanovesicles generated by porphyrin bilayers for use as multimodal biophotonic contrast agents. *Nat. Mater.* **10**, 324-332.
- 28) Raino, G., Stoferle, T., Park, C., Kim, H., Chin, I., Miller, R., Mahrt, R. (2010) Dye Molecules Encapsulated in a Micelle Structure: Nano-Aggregates with Enhanced Optical Properties. *Adv Mater.* **22**, 3681-3684.
- 29) Loo, C.; Lin, A.; Hirsch, L. R.; Lee, M. H.; Barton, J.; Halas, N. J.; West, J. L.; Drezek, R. (2004) Nanoshell-enabled photonics-based imaging and therapy of cancer. *Technol Cancer Res Treat.* **3**, 33-40.
- 30) Lal, S.; Clare, S. E.; Halas, N. J. (2008) Nanoshell-enabled photothermal cancer therapy: Impending clinical impact. *Acc Chem Res.* **41**, 1842-1851.
- 31) Hirsch, L. R., Stafford, R. J., Bankson, J. A., Sershen, S. R., Rivera, B., Price, R. E., Hazle, J. D., Halas, N. J., and West, J. L. (2003) Nanoshell-mediated Near-infrared Thermal Therapy of Tumors Under Magnetic Resonance Guidance. *Proc Natl Acad Sci U S.* **100**, 13549-13554.

- 32) Nanospectra Biosciences, Inc. Efficacy study of AuroLase therapy in subjects with primary and/or metastatic lung tumors. Available from:
<https://clinicaltrials.gov/ct2/show/NCT01679470>
- 33) Nanospectra Biosciences, Inc. Pilot study of AuroLase therapy in refractory and/or recurrent tumors of the head and neck. Available from:
<https://clinicaltrials.gov/ct2/show/NCT00848042>
- 34) Maltzahn, G. v.; Park, J.-H.; Agrawal, A.; Bandaru, N. K.; Das, S. K.; Sailor, M. J.; Bhatia, S. N. (2009) Computationally guided photothermal tumor therapy using long-circulating gold nanorod antennas. *Cancer Res.* **69**, 3892.
- 35) Roy I, Ohulchanskyy TY, Pudavar HE, Bergey EJ, Oseroff AR, Morgan J, Dougherty TJ, Prasad PN. (2003) Ceramic-based nanoparticles entrapping water-insoluble photosensitizing anticancer drugs: a novel drug-carrier system for photodynamic therapy. *J Am Chem Soc.* **125**, 7860–7865.
- 36) Pantarotto D, Singh R, McCarthy D, Erhardt M, Briand JP, Prato M, Kostarelos K, Bianco A. (2004) Functionalized carbon nanotubes for plasmid DNA gene delivery. *Angew Chem Int Ed Engl.* **43**, 5242–5246
- 37) Bhumkar DR, Joshi HM, Sastry M, Pokharkar VB. (2007) Chitosan reduced gold nanoparticles as novel carriers for transmucosal delivery of insulin. *Pharm Res.* **24**, 1415–1426.
- 38) Bagalkot V, Zhang L, Levy-Nissenbaum E, Jon S, Kantoff PW, Langer R, Farokhzad OC. (2007) Quantum dot-aptamer conjugates for synchronous cancer imaging, therapy, and sensing of drug delivery based on bi-fluorescence resonance energy transfer. *Nano Lett.* **7**, 3065–3070.

- 39) Hwu JR, Lin YS, Josephrajan T, Hsu MH, Cheng FY, Yeh CS, Su WC, Shieh DB. (2009) Targeted Paclitaxel by conjugation to iron oxide and gold nanoparticles. *J Am Chem Soc.* **131**, 66–68.
- 40) Cheng, L., Wang, C., Feng, L., Yang, K., Liu, Z. (2014) Functional Nanomaterials for Phototherapies of Cancer. *Chem Rev.* **114**, 10869-10939.
- 41) Yang, J., Choi, J., Bang, D., Kim, E., Lim, E.-K., Park, H., Suh, J.S., Lee, K., Yoo, K.H., Kim, E.K., Huh, Y.M., Haam, S. Angew. (2011) Convertible organic nanoparticles for near-infrared photothermal ablation of cancer cells. *Chem Int Ed.* **50**, 441.
- 42) Cheng, L.; Yang, K.; Chen, Q.; Liu, Z. (2012) Organic Stealth Nanoparticles for Highly Effective in Vivo Near-Infrared Photothermal Therapy of Cancer. *ACS Nano.* **6**, 5605.
- 43) Augustin, E., Czubek, B., Nowicka, A.M., Kowalczyk, A., Stojek, Z., Mazerska, Z. (2016) Improved cytotoxicity and preserved level of cell death induced in colon cancer cells by doxorubicin after its conjugation with iron-oxide magnetic nanoparticles. *Toxicol in Vitro.* **33**, 45-53.
- 44) Zhao, X., Yang, K., Zhao, R., Ji, T., Wang, X., Yang, X., Zhang, Y., Cheng, K., Liu, S., Hao, J., Ren, H., Leong, K., Nie, G. (2016) Inducing enhanced immunogenic cell death with nanocarrier-based drug delivery systems for pancreatic cancer therapy. *Biomaterials.* **102**, 187-197.
- 45) Mehtala JG, Torregrosa-Allen S, Elzey BD, Jeon M, Kim C, Wei A. (2014) Synergistic effects of cisplatin chemotherapy and gold nanorod-mediated hyperthermia on ovarian cancer cells and tumors. *Nanomedicine.* **9**, 1939–1955.

- 46) Liu, D., Ma, L., An, Y., Li, Y., Liu, Y., Wang, L., Guo, J., Wang, J., Zhou, J. (2016) Thermoresponsive Nanogel-Encapsulated PEDOT and HSP70 Inhibitor for Improving the Depth of the Photothermal Therapeutic Effect. *Adv Funct Mater.* DOI: 10.1002/adfm.201600031.
- 47) Alkilany, A.M., Thompson, L.B., Boulos, S.P., Sisco, P.N., Murphy, C.J. (2012) Gold nanorods: Their potential for photothermal therapeutics and drug delivery, tempered by the complexity of their biological interactions. *Adv Drug Deliv Rev.* **64**, 190-199.
- 48) Hahn GM, Braun J, Har-Kedar I. (1975) Thermochemotherapy: Synergism between hyperthermia and adriamycin (or bleomycin) in mammalian cell inactivation. *Proc Natl Acad Sci U S A.* **72**, 937-940.
- 49) Pedrosa, P., Vinhas, R., Fernandes, A., Baptista, P. (2015) Gold Nanotheranostics: Proof-of-Concept or Clinical Tool? *Nanomater.* **5**, 1853-1879.
- 50) Shen, S.; Tang, H.; Zhang, X.; Ren, J.; Pang, Z.; Wang, D.; Gao, H.; Qian, Y.; Jiang, X.; Yang, W. (2013) Targeting mesoporous silica-encapsulated gold nanorods for chemo-photothermal therapy with near-infrared radiation. *Biomater.* **34**, 3150.
- 51) Gong, H., Cheng, L., Xiang, J., Xu, H., Feng, L., Shi, X., Liu, Z. (2015) Stimulation of immune systems by conjugated polymers and their potential as an alternative vaccine adjuvant. *Adv Funct Mater.* **23**, 6059.
- 52) Duprez, L., Wirawan, E., Vanden Berghe, T., Vandenabeele, P. (2009) Major cell death pathways at a glance. *Microbes Infect.* **11**, 1050-1062.

- 53) Tait, S.W., Ichim, G., Green D.R. (2014) Die another way – non-apoptotic mechanisms of cell death. *J Cell Sci.* **127**, 2135-2144
- 54) Zhivotovsky, B., Orrenius, S. (2010) Cell cycle and cell death in disease: past, present and future. *J Intern Med.* **268**, 395-409.
- 55) Elmore, S. (2007) Apoptosis: A Review of Programmed Cell Death. *Toxicol Pathol.* **35**, 495–516.
- 56) Krysko, D.V., Berghe, T.V., Parthoens, E., D’Herde, K., Vandenabeele, P. (2008) Methods for distinguishing apoptotic from necrotic cells and measuring their clearance. *Meth Enzymol.* **442**, 307-341.
- 57) Adams, J. M., Cory, S. (2007) Bcl-2-regulated Apoptosis: Mechanism and Therapeutic Potential. *Curr Opin Immunol.* **19**, 488–496.
- 58) Pattani, V., Shah, J., Atalis, A., Sharma, A., Tunnel, J. (2015) Role of apoptosis and necrosis in cell death induced by nanoparticle-mediated photothermal therapy. *J Nanopart Res.* **17**, 20
- 59) Perez-Hernandez, M., del Pino, P., Mitchell, S.G., Moros, M., Stepien, G., Pelaz, B., Parak, W.J., Galvez, E.M., Pardo, J., de la Fuente, J.M. (2015) Dissecting the molecular mechanism of apoptosis during photothermal therapy using gold nanoprisms. *ACS Nano.* **9**, 52–61.
- 60) Boya, P., Kroemer, G. (2008) Lysosomal Membrane Permeabilization in Cell Death. *Oncogene.* **27**, 6434–6451.
- 61) Konstantinidis K, Whelan RS, Kitsis RN. (2012) Mechanisms of Cell Death in Heart Disease. *Arterioscler Thromb Vasc Biol.* **32**, 1552-1562.

- 62) McKeague, A.L., Wilson, D.J., Nelson, J. (2003) Staurosporine-induced apoptosis and hydrogen-peroxide-induced necrosis in two human breast cell lines. *Br J Cancer*. **88**, 125-131.
- 63) Melamed JR, Edelstein RS, Day ES. (2015) Elucidating the fundamental mechanisms of cell death triggered by photothermal therapy. *ACS Nano*. **9**, 6–11.
- 64) Li, X., Naylor, M.F., Le, H., Nordquist, R.E., Teague, K., Howard, A., Murray, C., Chen, W.R. (2010) Clinical effects of in situ photoimmunotherapy on late-stage melanoma patients. *Cancer Biol Ther*. **10**, 1081-1087.
- 65) Xu, P., Gullotti, E., Tong, L., Highley, C., Errabelli, D., Hasan, T., Cheng, J., Kohane, D., Yeo, Y. (2009) Intracellular drug delivery by poly(lactic-co-glycolic acid) nanoparticles, revisited. *Mol Pharm*. **6**, 190-201.
- 66) Kroemer, G., Galluzzi, L., Kepp, O., Zitvogel, L. (2013) Immunogenic cell death in cancer therapy. *Annu Rev Immunol*. **31**, 51e72.
- 67) Krysko, D., Garg, A., Kaczmarek, A., Krysko, O., Agostinis, P., Vandenabeele, P. (2012) Immunogenic cell death and DAMPs in cancer therapy. *Nat Rev Cancer* **12**, 860e875.
- 68) Casares, N., Pequignot, M., Tesniere, A., Ghiringhelli, F., Roux, S., Chaput, R. (2005) Caspase-dependent immunogenicity of doxorubicin-induced tumor cell death. *J Exp Med*. **202**, 1691e1701.